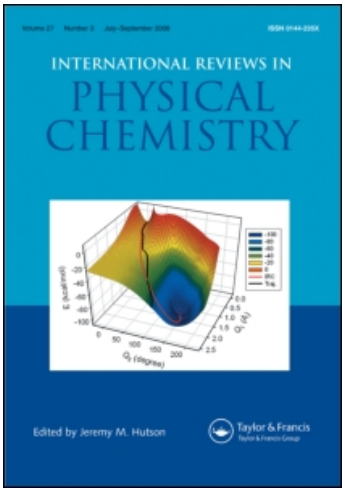

International Reviews in Physical Chemistry
Publication details, including instructions for authors and subscription information:
http://www.informaworld.com/smpp/title~content=t713724383

Spectroscopy and dynamics of hydride radical van der Waals complexes

Michael C. Heaven[a]
[a] Department of Chemistry, Emory University, Atlanta, GA 30322, USA

To cite this Article Heaven, Michael C.(2005) 'Spectroscopy and dynamics of hydride radical van der Waals complexes', International Reviews in Physical Chemistry, 24: 3, 375 — 420
To link to this Article: DOI: 10.1080/01442350500353092
URL: http://dx.doi.org/10.1080/01442350500353092

International Reviews in Physical Chemistry,
Vol. 24, Nos. 3–4, July–December 2005, 375–420

Taylor & Francis
Taylor & Francis Group

Spectroscopy and dynamics of hydride radical van der Waals complexes

MICHAEL C. HEAVEN*

Department of Chemistry, Emory University, Atlanta, GA 30322, USA

(*Received 16 August 2005; in final form 13 September 2005*)

Spectroscopic and theoretical studies of hydride radical–rare gas atom complexes (Rg–HX) are reviewed. This family of van der Waals molecules is of interest as they can be used to explore the characteristics of the long-range forces associated with open-shell species. Orbitally degenerate states of HX radicals have an electronic anisotropy that results in van der Waals interactions that are qualitatively different from those exhibited by the corresponding closed-shell systems. Rg–HX complexes, where X is a first- or second-row *p*-block element, reveal systematic trends where the anisotropic components of the physical interactions are determined by the electronic orbital configuration. Radicals in Σ, Π and Δ states with singlet, doublet and triplet spin multiplicities have been examined. When Rg = He, Ne or Ar the interaction potential energy surfaces can be predicted using high-level *ab initio* methods. Theoretical studies have established the methods and basis sets that are capable of providing an accurate description of the long-range forces for open-shell molecules. Clusters consisting of an HX molecule with multiple rare gas atoms are model systems for studies of solvated radicals. Potential energy surfaces derived from the binary clusters are being used to construct approximate potentials for Rg_n–HX clusters. The equilibrium structures and vibrational dynamics predicted for these systems show that solvated radicals exhibit unique properties.

Contents

*Email: mheaven@emory.edu

International Reviews in Physical Chemistry
ISSN 0144–235X print/ISSN 1366–591X online
http://www.tandf.co.uk/journals
DOI: 10.1080/01442350500353092

1. Introduction

The long-range interactions between a radical and a closed-shell molecule or atom are of interest from a number of perspectives. If the interaction leads to a chemical reaction, the long-range forces can influence the approach of the reactants to the transition state and the energy partitioning as the products depart. The Cl+HD reaction provides a dramatic example of the influence that the attractive van der Waals forces can exert on reaction dynamics. Skouteris *et al.* [1] have shown that the propensity to form DCl at near-threshold collision energies cannot be correctly modelled without considering the van der Waals region of the potential energy surfaces. The outcome of an inelastic collision will also be determined by the details of the intermolecular forces. Due to the coupling of electronic and nuclear degrees of freedom in these events, collisional energy transfer involving open-shell molecules is a richer and more complex phenomenon than the closed-shell equivalent [2–7]. The key to understanding reactive and inelastic collision dynamics is knowledge of the interaction potentials. Consequently, a great deal of experimental and theoretical effort has been directed towards the determination of potential energy surfaces for prototypical collision pairs. Investigations of the interactions between diatomic radicals and rare gas atoms have proved to be particularly fruitful as these systems are both experimentally convenient and theoretically tractable. From the experimental side, there are two complementary methods used to probe potential energy surfaces. These are state resolved measurements of inelastic collision dynamics and spectroscopic studies of van der Waals molecules. The present review is focused on the latter, and is further restricted to the topic of diatomic hydride radicals (HX) interacting with rare gas atoms (Rg). This family of complexes provides valuable insights concerning the characteristic properties of long-range forces associated with open-shell molecules. Although these are not reactive systems, the rare gas atoms act as useful probes of the way in which a particular radical responds in physical interactions (e.g. the influence of polarizability, dispersion interactions, exchange repulsion, etc.). For example, studies of $CH(X)$+He interactions have provided a framework for understanding the long-range component of $CH(X)+H_2$ collisions [7, 8]. Theoretical potential energy surfaces for Rg–HX pairs can be calculated using high-level *ab initio* electronic structure methods. The techniques used to compute accurate long-range potentials for open-shell systems are being thoroughly examined and refined through the studies of Rg–HX complexes. Additional interest in He+HX interactions has been stimulated by two recent developments. The first is the work on the spectroscopy and dynamics of molecules and atoms trapped in large He droplets [9–11]. HX radicals are an excellent choice for studies of pre-reactive complexes and low-temperature reaction dynamics

in this medium. Secondly, it has been recognized that HX radicals may be cooled to ultra-low temperatures using magneto-optical traps [12]. One scheme for trap loading involves ^{3}He buffer gas cooling [13]. The applicability of this approach is critically dependent on the details of the He–HX potential energy surfaces [14, 15].

Studies of HX radicals clustered with multiple rare gas atoms are also considered in this review. These clusters are models systems for solvated radicals and knowledge of their properties facilitates the interpretation of the spectroscopy and dynamical behaviour of HX radicals trapped in rare gas solids. Once the potential energy surfaces for a Rg–HX pair are known, data for clusters that contain multiple rare gas atoms can be used to examine the many-body forces that contribute to the potential energy of the composite system. This progression has been demonstrated in an elegant series of experimental and theoretical studies for closed-shell Ar_n–HF clusters [16–21]. The issue of non-additive forces for open-shell complexes has yet to be addressed in such a detailed and systematic fashion. There are interesting subtleties for the open-shell Rg_n–HX complexes that are unique. For example, Xu *et al.* [22] have drawn attention to the fact that even the basic sum of pair-potentials model is non-additive if the radical is in an orbitally degenerate electronic state.

Recent reviews concerning open-shell complexes include the work by Kim and Meyer on Rg–NO [23], Wheeler *et al.* on OH–H_2 [24] and Carter *et al.* [25] on Rg–HX complexes with Rg = Ne, Ar, and Kr and X = O or S. The electronic structure methods used to calculate the properties of open-shell complexes have been reviewed by Chalasinski *et al.* [8, 26] The present review is mostly concerned with recent progress on the Rg–HX complexes, but the results have been organized to illustrate periodic trends. Hence a discussion of earlier work is included where relevant. The organization of this review is as follows. The next two sections present brief summaries of the techniques used to observe Rg–HX complexes, the models used to analyse the spectra, and the methods for refining potential energy surfaces through direct fitting to spectroscopic data. The results for binary Rg–HX are presented in section 4. These have been organized in order of the periodic group for X. Within each subgroup the order of the discussion is somewhat chronological, often starting with the Ar complexes as these are generally the most heavily studied. Section 5 describes work on the clusters with multiple rare gas atoms. Although there is very little experimental data for this topic, the intriguing dynamical behaviour predicted by large-scale theoretical calculations is of interest in its own right, and should stimulate further experimental studies of these clusters.

2. Experimental methods

Rg–HX complexes are generated in low-temperature supersonic expansions [27]. The radicals are obtained using photolysis or electric discharge dissociation of a stable precursor molecule (e.g. OH from photolysis of HO–NO_2 or discharge fragmentation of H_2O [28, 29]). In most instances the radical fragments are created in the high gas density region of the expansion, and they cool and form complexes as the expansion evolves. However, Mackenzie *et al.* [30, 31] have observed SH–Ar when SH_2–$Ar_{n\leq 2}$ complexes were photodissociated under near collision-free conditions. Relatively low number densities of complexes are formed by these methods,

so techniques with high sensitivity are needed for spectroscopic characterizations. Laser induced fluorescence (LIF) of electronic transitions has been widely used for this purpose. As pulsed methods of radical complex production have proved to be most effective, pulsed excitation has been applied. Conventional pulsed dye lasers can be operated with sufficiently narrow linewidths (around $0.06\,cm^{-1}$) to resolve the rotational structure when the complexing agent is a rare gas atom or a small molecule. To achieve higher resolution, Miller and co-workers [25, 32] and Schleipen *et al.* [33] used pulse amplified ring dye lasers. They were able to resolve the nuclear hyperfine structure of OH–Rg and SH–Rg complexes (spectra recorded with an effective linewidth of $0.008\,cm^{-1}$ in the near-UV). Even at the highest resolution, the electronic spectra can pose challenging analysis problems, particularly if both the ground and excited states are orbitally degenerate for the monomer. Fluorescence depletion techniques have proved to be valuable as a means to establish unique rotational line assignments.

LIF of jet-cooled complexes is well suited for studies of electronically excited states, but the data obtained for the ground states is limited (usually just the molecular constants for the zero-point vibrational level). Provided that the electronically excited state of the complex does not undergo rapid predissociation, dispersed fluorescence and stimulated emission pumping (SEP) techniques can be used to observe vibrationally excited levels of the ground state. In particular, Lester and co-workers [34–36] have been successful in applying SEP to characterize the ground states of OH–Ne and OH–Ar. This group has also pioneered the use of IR–optical double resonance measurements to obtain high-resolution infrared spectra for OH complexes [37, 38]. Both fluorescence depletion and sequential excitation methods have been applied to obtain IR spectra. The most accurate data for ground state complexes has been obtained from microwave measurements. Endo and co-workers have examined the microwave spectra of OH and SH rare gas complexes using pulsed Fourier transform techniques [28, 29, 39–42].

3. Theoretical considerations

The objective of most spectroscopic studies of Rg–HX complexes has been the determination of potential energy surfaces for the van der Waals interactions. The complex of a radical in a non-degenerate electronic state is characterized by a single potential energy surface. When the radical is in an orbitally degenerate state the degeneracy is lifted for non-linear geometries of the complex, and the interactions can be described using two adiabatic potential energy surfaces. For example, consider the $X^2\Pi$ state of CH, which is derived from the $3\sigma^2 1\pi$ electronic configuration. The 1π orbitals are primarily C $2p_x$ and $2p_y$. A rare gas atom approaching along the axis of the unfilled $p\pi$ orbital will experience less repulsion than an atom approaching along the half-filled orbital. The point group is lowered to C_s, and the Π state splits into electronic states of A'' and A' symmetry [6, 7, 43–45]. For CH(X)–Rg the A'' potential energy surface, which has the unfilled orbital in the plane of reflection, has a relatively deep minimum for side-on approach and a strongly bent equilibrium structure. In contrast, the A' surface is much less attractive and less anisotropic. This situation is illustrated by the two-dimensional potential energy surface contours for CH(X)–Ne

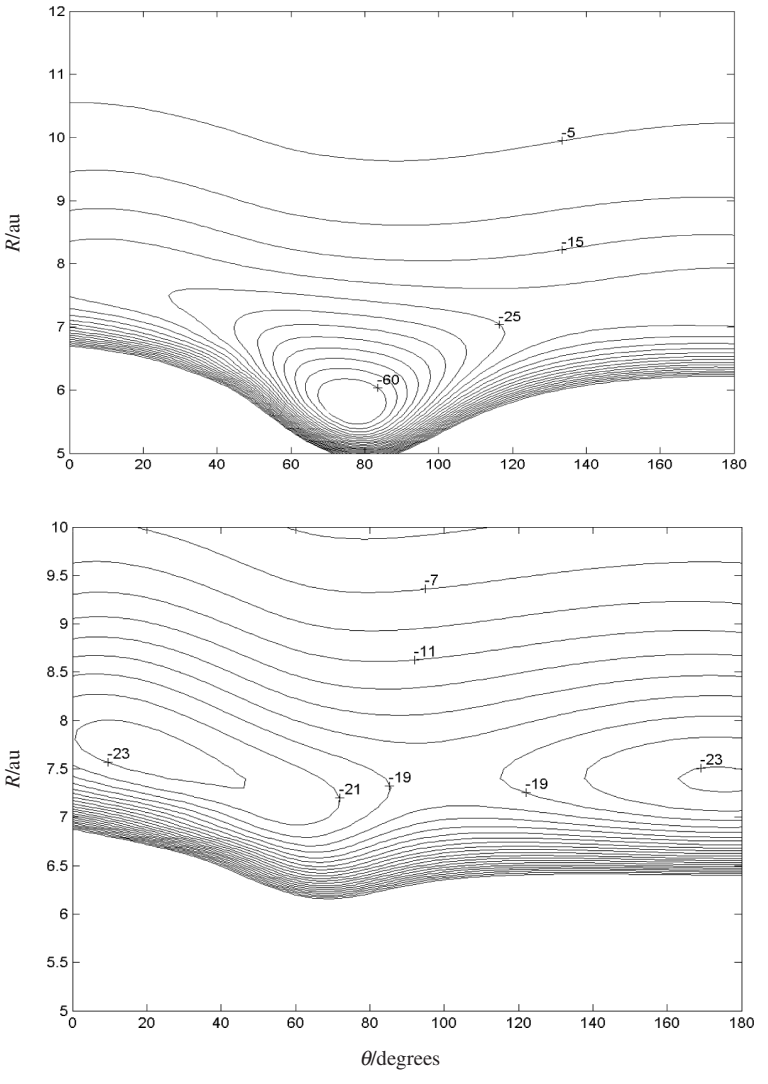

Figure 1. Contour plots of the *ab initio* potential energy surfaces for CH($X\,^2\Pi$)–Ne. The energies of selected contours are indicated in cm^{-1} units, relative to the CH($X\,^2\Pi$)+Ne dissociation asymptote. The upper and lower traces correspond to states of A'' and A' reflection symmetry, respectively. The contour lines for the A'' surface are drawn at $5\,cm^{-1}$ intervals, while those for the A' surface are spaced by $2\,cm^{-1}$.

shown in figure 1. For these plots, and throughout the following discussion of Rg–HX complexes, Jacobi coordinates have been employed. These are defined by r, the H–X distance, R, the distance between Rg and the HX centre of mass, and, θ the angle between r and R. The linear complex with Rg bound to the H atom side of the diatom corresponds to $\theta = 0^\circ$.

As discussed in the following sections, the $p\pi$ orbital occupation exerts a strong influence on the equilibrium structures of Rg–HX complexes. Electronic structure calculations indicate that this is primarily an exchange repulsion effect for Rg = He

through Kr. When an empty $p\pi$ orbital is available, potential energy surfaces that are qualitatively similar to those of figure 1 are encountered. Configurations with two or more electrons in the $p\pi$ orbitals usually produce surfaces with linear minima. The typical form for surfaces of this type is illustrated in figure 2 by the contour diagrams for the $A^2\Delta$ state of CH–Ne, which is derived from the $3\sigma 1\pi^2$ configuration.

Spectroscopic data for triatomic complexes cannot be inverted to determine the potential energy surfaces. While the RKR inversion procedure provides a direct path from the spectroscopic constants to the potential energy curve for a diatomic molecule, there is no equivalent transformation for a polyatomic system. Instead, model surfaces are tested and refined through forward convolution. There is a close interplay between theory and experiment here, as the guidance provided by theoretical calculations is often needed to achieve a satisfactory analysis of the spectrum. There are a number of useful approximations that simplify the task of calculating the properties of Rg–HX systems. First is the decoupling of H–X vibrational motion from the soft van der Waals motions. As the HX vibrational frequencies are much greater than the frequencies of the van der Waals bending and stretching modes, it is reasonable to consider two-dimensional Rg–HX potential energy surfaces with the H–X distance frozen at the vibrationally averaged value. The Hamiltonian for Rg–HX complexes can then be written as [46–49]

$$\hat{H} = \hat{T} + V + \hat{h} \tag{1}$$

where $\hat{T}$ is the intermolecular nuclear kinetic, V is the interaction potential energy surface (or surfaces) and $\hat{h}$ is the Hamiltonian operator for the diatom. The kinetic energy operator consists of two parts: the radial stretch and the end-over-end rotation,

$$\hat{T} = -\frac{\partial^2}{2\mu\partial R^2} + \frac{\left(\hat{J} - \hat{j}\right)^2}{2\mu R^2} \tag{2}$$

(in atomic units) where μ is the reduced mass of the complex, $\boldsymbol{J}$ is the total angular momentum of the complex and $\boldsymbol{j}$ is the angular momentum of the diatom. Once the vibrational motion of H–X has been factored out, it is possible to work with just the roto-electronic part of $\hat{h}$ using vibrationally averaged values for the molecular constants. To a first approximation the reduced form of $\hat{h}$ can then be written as

$$\hat{h} = a_{\mathrm{SO}}\,\hat{\mathcal{L}} \cdot \hat{s} + b\left(\hat{j} - \hat{\mathcal{L}} - \hat{s}\right)^2 \tag{3}$$

where $\hat{\mathcal{L}}$ is the electronic angular momentum operator, $\hat{s}$ is the spin operator, a_{SO} is the spin–orbit coupling constant and b is the diatomic rotational constant. The bound energy levels for a given potential energy surface (or pair of surfaces) can be found by variational calculations or solution of the close coupling equations using a suitable set of basis functions. For the complexes considered here, model calculations show that the diatom is not strongly perturbed by the interaction with

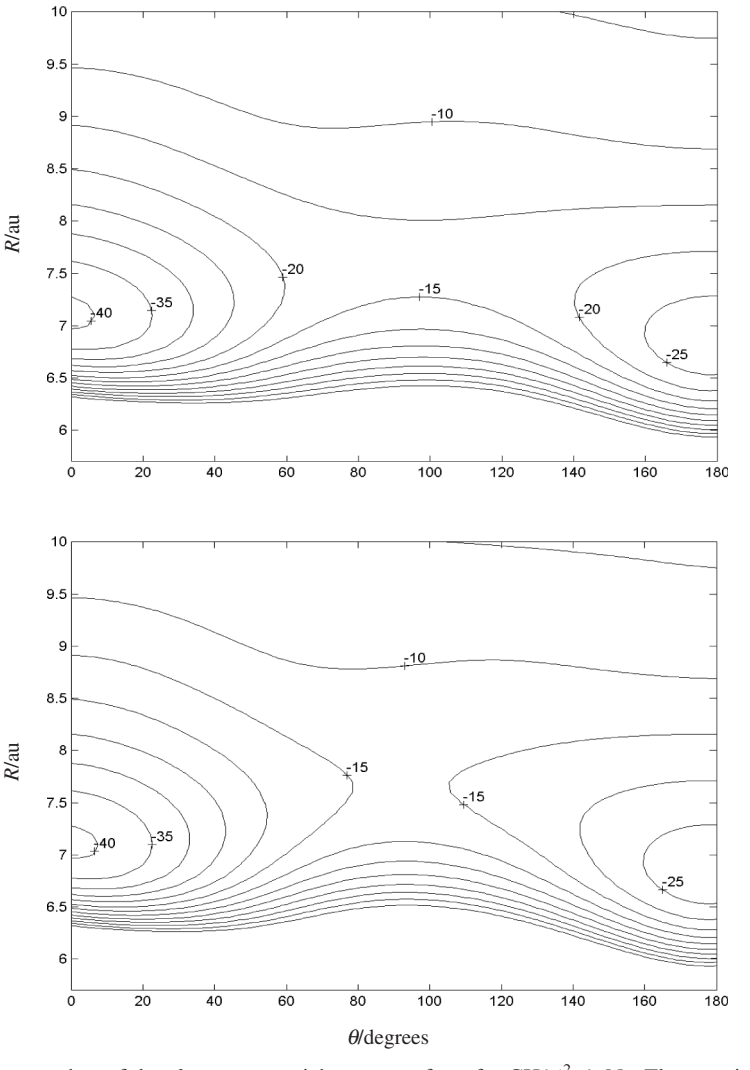

Figure 2. Contour plots of the *ab initio* potential energy surfaces for CH($A^2\Delta$)–Ne. The energies of selected contours are indicated in cm^{-1} units, relative to the CH($A^2\Delta$)+Ne dissociation asymptote. The contour lines are drawn at $5\,cm^{-1}$ intervals. The upper and lower traces correspond to states of A' and A'' reflection symmetry, respectively.

the Rg partner. Consequently, the diatomic quantum numbers provide useful state labels for the complex. Following the convention of Dubernet *et al.* [46] and others, the properties of the HX radical are designated using lower case quantum labels, while upper case labels are given for states of the entire complex. The most useful quantum labels are collected and defined in table 1.

High-level *ab initio* calculations are used to obtain the first estimates for the potential energy surfaces. Two-dimensional potentials are generated for a grid of θ_i and R_i values. The grids may be evenly spaced or distributed over quadrature points. Note that

Table 1. Definitions of quantum number labels for open-shell triatomic complexes.

Quantum number	Description
Definitions for the diatom[a]	
v	H–X vibration.
λ	projection of electronic orbital angular momentum along the diatomic axis.
s	spin angular momentum.
σ	projection of $\boldsymbol{s}$ on the diatomic axis.
r	rotational angular momentum.[b]
n	sum of orbital and rotational angular momentum ($\boldsymbol{r}+\boldsymbol{\lambda}$).
j	total angular momentum of diatom.
ω	projection of $\boldsymbol{j}$ on the diatomic axis ($\boldsymbol{\sigma}+\boldsymbol{\lambda}$).
Definitions for the complex[a]	
v_c	Rg–HX stretching vibration.
L	end-over-end rotational angular momentum of the complex.
N	sum of orbital and rotational angular momentum ($\boldsymbol{L}+\boldsymbol{n}$).
K	projection of $\boldsymbol{n}$ on the body-fixed axis.[c]
P	projection of $\boldsymbol{j}$ on the body-fixed axis.[c]
J	total angular momentum.

[a]Boldface type is used to designate vector quantities.
[b]r is used for both the rotational angular momentum and the Jacobi coordinate. The appropriate definition is apparent from the context of use.
[c]For large anisotropies the projection of the angular momentum along R remains reasonably well defined, but n or j are no longer useful quantum numbers.

ab initio calculations for orbitally degenerate states yield the adiabatic A' and A'' potential energy surfaces described above. This is not the best representation for most dynamical calculations. As discussed by Alexander [4], it is more convenient to express the potential energy surfaces in terms of the diabatic average $V_{\rm ave} = (V_{A'} + V_{A''})/2$ and difference $V_{\rm diff} = (-1)^{\lambda}(V_{A'} - V_{A''})/2$ potentials. For the difference potential, $\lambda = 1, 2, 3, \ldots$ indicates the spatial symmetry of the diatomic electronic state, Π, Δ, Φ, etc. Spline fits, interpolations, or quadrature techniques may then be used in calculating matrix elements of the potential energy surfaces. Numerical solutions of the Hamiltonian given by equation (1) may be simplified by expanding the potential energy surfaces in terms of Legendre polynomials. This permits the use of analytical expressions for the angular components of the potential energy matrix elements. The average and difference potentials are represented by the expressions [46–48]

$$V_{\rm ave}(R,\theta) = \sum_{l=0}^{l_{\rm max}} V_{l0}(R) P_{l0}(\cos\theta) \tag{4}$$

and

$$V_{\rm diff}(R,\theta) = \sum_{l\geq m}^{l_{\rm max}} V_{lm}(R) P_{lm}(\cos\theta) \tag{5}$$

where $V_{l0}(R)$ and $V_{lm}(R)$ are radially dependent expansion coefficients, P_{l0} are the regular Legendre polynomials and P_{lm} are the associated Legendre polynomials with $m = 2\lambda$.

If all of the terms in the Hamiltonian defined by equation (1) are retained, large matrices are required to obtain converged energy levels. Eliminating the off-diagonal elements that arise from the $(\hat{J}-\hat{j})^2$ term of equation (2) can considerably reduce the size of the matrices [47]. This is most easily seen by considering the calculation with body-fixed basis functions, where the projection of the diatomic angular momentum on the R-axis is given by P or K (see table 1). The $\hat{J}\cdot\hat{j}$ part of this operator mixes basis states with different values of P or K (this is often referred to as a Coriolis interaction) [50]. Provided that the interacting pair of P or K states are not too close in energy, the interaction is weak and may be neglected by eliminating the off-diagonal matrix elements of $\hat{J}\cdot\hat{j}$ (centrifugal decoupling (CD) approximation).

So far we have simplified the eigenvalue problem by uncoupling the diatomic vibrational motion and eliminating the Coriolis term. Uncoupling of the radial and angular motions also proves to be a relatively good approximation in many instances. This is accomplished by constructing 'adiabatic bender' potentials [47]. Single-point energies are generated by diagonalizing the Hamiltonian matrix with the radial coordinate frozen. Calculations repeated at a series of R-values define one-dimensional potentials that are suitably averaged over the angular motions. Energy levels for the complex are then found by solution of the radial Hamiltonian for each adiabatic bender potential. Apart from their utility in low-cost exploratory calculations, the adiabatic bender potentials are of value as they often yield physical insights concerning the energy level structure of the complex. Dubernet *et al.* [46] took this process a step further by considering the solutions of equation (1) with both r and R frozen. Effective one-dimensional angular potentials were examined and a series of correlation diagrams were developed for the bending/internal rotation energy levels for complexes in $^2\Sigma$, $^1\Pi$, $^2\Pi$ and $^3\Pi$ states. The evolution of the energy levels was followed as a function of the ratio V_{20}/b, where b is the diatomic rotational constant. The effect of breaking the symmetry of the anisotropy by including a V_{10} term was also explored. Dubernet *et al.*'s [46] correlation diagrams provide insights that have greatly facilitated the understanding and interpretation of the bending energy level structures. Another valuable component of this study was a formal discussion of angular momentum coupling in open-shell complexes. Dubernet *et al.* [46] defined limiting coupling cases labelled A, B and C that are analogous to Hund's coupling cases a, b and c for linear molecules.

Manageably sized *ab initio* calculations are not presently capable of producing van der Waals potential energy surfaces that can accurately reproduce spectroscopic data. Hence, the theoretical potential energy surfaces need to be adjusted in order to obtain quantitative agreement between the observed and calculated energy level patterns. To facilitate this process, analytical representations of the surfaces are generated. There are several options for the method used to fit potential energy surfaces. For some of the earliest studies of OH–Rg complexes, a flexible potential energy function was developed by Bowman *et al.* [51, 52]. This was defined by generalized Morse function fits to radial cuts through the potential at $\theta=0$, 90 and 180°. Angle-dependent switching functions were used to construct the entire surface from these cuts. The approach favoured by Alexander, Dagdigian and co-workers [44, 47, 53–55] involves fitting fixed angle (θ_i) slices through the potential to obtain unique sets of radial parameters for each cut. Hutson [56] has defined potentials

where the parameters of the radial functions are expanded in terms of low-order polynomials of the angle θ. Alternatively, fixed radius angular cuts through the surface can be fitted to associated Legendre polynomial expansions to obtain values of $V_{l0}(R_i)$ and $V_{lm}(R_i)$ for the i-th radial distance. These pointwise potentials are then fitted to standard expressions such as Morse or generalized Morse functions [57, 58].

Ab initio calculations for Rg–HX complexes typically underestimate the binding energy and overestimate the Rg–HX equilibrium bond length. Apart from these defects, the qualitative shape of the surface is usually correct. The theoretical potentials can be significantly improved by scaling (to adjust the bond energy) and translation along the R-coordinate (to adjust the rotational constants). Several schemes have been devised that permit systematic scaling and translation of a reference potential energy surface [40, 41, 44, 47, 59, 60].

4. Binary complexes

4.1. *BH–Ar and AlH–Ar*

LIF spectra for the $A^1\Pi$–$X^1\Sigma^+$ transition of BH–Ar were reported by Hwang *et al.* [61]. The radical was produced by 193 nm photolysis of diborane. Twelve sharp bands of BH–Ar were found in association with the monomer 0–0 band. The origin band was red-shifted from the monomer parent line by 84 cm^{-1}, which defines the difference in the binding energies $D_0' - D_0''$. Diffuse bands were seen at energies more than 92 cm^{-1} above the origin. Rotational analyses were carried out for 10 of the sharp bands. Assignment of the vibronic structure was guided by the theoretical calculations of Alexander *et al.* [47]. *Ab initio* potential energy surfaces were calculated using a multi-reference configuration interaction method (MR–CI(D)) with a quadruple zeta quality basis set (*avqz-f*). The full counterpoise (CP) correction was applied. The potential energy surfaces yielded bent equilibrium structures for the ground and excited states (the equilibrium coordinates and well depths are listed in table 2). This was consistent with the fact that the ground and excited states are derived from the $3\sigma^2$ and $3\sigma 1\pi$ configurations, so that approach of the Ar atom along the axis of an unfilled $p\pi$ orbital is possible for both states. The pronounced differences in the $V_{A'}$ and $V_{A''}$ potential energy surfaces of BH(A)–Ar are evident from the stationary point data presented in table 2. Bound state calculations showed that the *ab initio* surfaces were too shallow, with R_e values that were too large [47]. For example, the calculated properties of BH(X)–Ar were $D_0 = 29$ and $B_0 = 0.103$ cm^{-1}, as compared to the observed values of $D_0 = 92$ and $B_0 = 0.133$ cm^{-1}. Scaling of the ground state potential by a factor of approximately 1.6 and inward translation along R by 0.5 au improved the predicted ground state properties ($D_0 = 69$ and $B_0 = 0.123$ cm^{-1}), but it was evident that larger changes in the potential would be needed to achieve quantitative agreement with the experimental results. Moderate adjustment of the A state potentials produced much better agreement with the spectroscopic data. Scaling by a factor of approximately 1.6 and inward shifting by about 0.3 au yielded predicted constants of $D_0 = 174$ and $B_0 = 0.164$ cm^{-1}, as compared to the measured values of $D_0 = 176$ and $B_0 = 0.167$ cm^{-1}.

Table 2. Stationary point data for BH–Ar and AlH–Ar complexes.

Surface	D_e/cm^{-1}	θ_e	R_e/au	Reference
BH($X^1\Sigma$)–Ar				
V, *ab initio*	125	74.0	6.70	[47]
V, modified	198	74.5	6.22	[47]
BH($A^1\Pi$)–Ar				
$V_{A'}$, *ab initio*	85	0.0	8.02	[47]
$V_{A'}$, *ab initio*	69	125.0	7.98	[47]
$V_{A''}$, *ab initio*	183	89.5	6.22	[47]
$V_{A'}$, modified	128	0.0	7.76	[47]
$V_{A'}$, modified	112	139.0	7.64	[47]
$V_{A''}$, modified	280	88.5	5.97	[47]
AlH($X^1\Sigma$)–Ar				
V, *ab initio*	154.7	72.7	7.17	[55]
V, modified	211.5	72.6	6.88	[55]
AlH($A^1\Pi$)–Ar				
$V_{A'}$, *ab initio*	80.4	0.0	9.25	[55]
$V_{A'}$, *ab initio*	76.7	150.9	8.51	[55]
$V_{A''}$, *ab initio*	198.2	80.8	6.86	[55]
$V_{A'}$, modified	130	0.0	8.90	[55]
$V_{A'}$, modified	125.4	152.5	8.19	[55]
$V_{A''}$, modified	321.2	80.5	6.54	[55]

The bending/internal rotation energy level structure of BH(A)–Ar is of particular interest. This structure is most easily understood by examining the correlation diagrams of Dubernet *et al.* [46] and the adiabatic bender potentials. Alexander *et al.* [47] have shown that the adiabatic bender model is a very good approximation for BH(A)–Ar. Their curves for the modified potential energy surfaces are shown in figure 3. All of the rotationally resolved bands were attributed to upper levels that correlated with the BH($A^1\Pi$, $j=1$) + Ar dissociation asymptote. The interaction with the Ar atom split the $j=1$ level of the diatom into states with $P'=0^-$, 1_l, 1_u, and 0^+ (in ascending energy order). Here, and in the following sections, the subscripts l and u are used to distinguish the lower and upper energy components of the two states for a given j parent state that have the same value for P. This convention is not applied to the $P=0$ states as they are differentiated by their symmetry properties (given as the +/− superscript). The transition from the zero-point level of BH(X)–Ar ($P=0^+$) to the lowest energy level of BH(A)–Ar ($P=0^-$) was not observed as it is electric-dipole forbidden. Transitions to the $P=1_l$, 1_u and 0^+ states were identified in the spectrum. Note that the 1_l curve in figure 3 is much deeper than the 1_u and 0^+ curves, and that the R_e value for 1_l is smaller. These trends were clearly reflected by the molecular constants observed for these states. Alexander *et al.* [47] were able to show that the $P=0^-$ and 1_l states behaved as if they belonged to the deeply bound $V_{A''}$ potential energy surface, while the weakly bound $P'=1_u$ and 0^+ states were associated with correlated motions on both $V_{A'}$ and $V_{A''}$.

Dagdigian, Alexander and co-workers [55, 62] also characterized the AlH–Ar complex via the 0–0 band of the $A^1\Pi$–$X^1\Sigma^+$ transition. For the experimental study AlH was generated by multiphoton dissociation of trimethylaluminum at 193 nm. Rotationally resolved spectra were recorded for 14 bands that exhibited sharp lines.

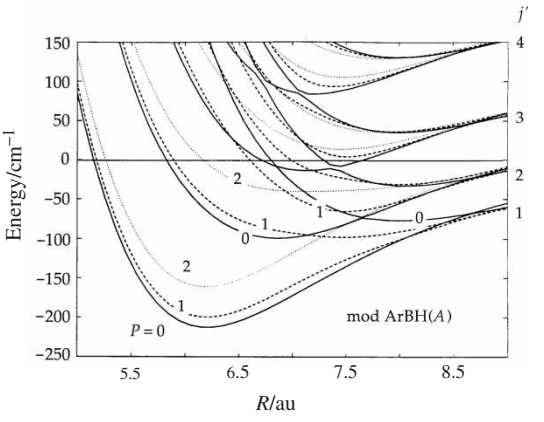

Figure 3. Radial adiabatic bender curves for BH($A^1\Pi$)–Ar calculated for the modified potential energy surface of Alexander *et al.* [47] for an effective angular momentum of $L=1$. The $P=0$, 1, and 2 potential curves associated with the monomer $j=1$, 2, 3, and 4 levels are shown. This figure is reproduced with permission from reference [47].

Several diffuse bands were also reported. As expected, the properties of AlH–Ar were very similar to those of BH–Ar. *Ab initio* potential energy surfaces for AlH(A, X)–Ar were calculated using the same level of theory that had been applied to BH–Ar (MR–CI(D)/*avqz–f*+CP). The resulting surfaces had the same qualitative features as those of BH–Ar, as can be seen from the stationary point data given in table 2, the primary difference being that the potential wells for AlH–Ar were deeper. To make bound state predictions that could be compared with the experimental data, the *ab initio* potentials were modified by increasing the well depths (by a factor of 1.6) and translating inward by approximately 0.3 au. Close coupling calculations with the modified potentials gave results that were in good agreement with the spectroscopic observations. The measured ground state constants of $D_0=124$ and $B_0=0.0687\,\mathrm{cm}^{-1}$ were reproduced to within the experimental uncertainty. For the A state the calculated constants for $P=1_l$ ($D_0=234$ and $B_0=0.0794\,\mathrm{cm}^{-1}$) were close to the experimental values ($D_0=220$ and $B_0=0.0785\,\mathrm{cm}^{-1}$). Transitions from an excited level of the ground state were observed in the AlH–Ar spectrum, which permitted further evaluation of the theoretical models. The lower excited level was assigned as $P=1_l$, $j=1$, located approximately $7\,\mathrm{cm}^{-1}$ above the $P=0^+$ zero-point level. The theoretical calculations for both BH(A)–Ar and AlH(A)–Ar predicted that the lowest energy state would be $P=0^-$, but this could not be verified for BH(A)–Ar due to the optical selection rules. The transition from $P=1_l$ to $P=0^-$ is allowed, and this was observed for AlH–Ar. In accordance with theory, the $P=0^-$ level was found below $P=1_l$. The AlH–Ar spectrum also contained transitions from excited state levels that correlated with the $j=2$ and 3 dissociation asymptotes. Overall, the theoretical calculations were successful in reproducing the ro-vibronic structure of AlH–Ar.

4.2. *CH–Rg complexes (Rg = He, Ne and Ar)*

The spectroscopy and dynamics of the CH radical have been studied extensively. Much of the interest has been driven by the importance of CH in combustion, atmospheric

chemistry, and astrophysics. CH has also proved to be a very useful prototype for studies of the inelastic collision dynamics of an open-shell molecule. A variety of spectroscopic techniques can be used to detect CH in the $X^2\Pi$, $A^2\Delta$ or $B^2\Sigma^-$ states, which facilitates comparisons of the dynamics for states with differing values for the axial projection of the electronic orbital angular momentum. From a theoretical perspective, the collisions of CH with rare gas atoms present the most tractable model systems [63–66]. To date, collisional energy transfer processes have been characterized for CH(X)+He [7], CH(X)+Ar [67, 68], CH(A)+He [69, 70], CH(A)+Ar [69–72], CH(B)+He [69, 70] and CH(B)+Ar [69, 70, 73]. Potential energy surfaces have been calculated for most of these combinations, and all show van der Waals minima at long-range.

The CH(X)–He complex has not been observed, but the potential energy surfaces for the CH(X)+He interaction were calculated for use in quantum inelastic scattering calculations. Wagner *et al.* [43] generated the $V_{A'}$ and $V_{A''}$ surfaces using CAS–SCF calculations with the *avtz* basis set. The $X^2\Pi$ state of CH is derived from the $3\sigma^2 1\pi$ electronic configuration, so the interactions with a rare gas atom were equivalent to those described above for BH($A^1\Pi$). Hence the $V_{A''}$ surface exhibited a van der Waals minimum for the bent geometry (with a well depth of about $30\,\mathrm{cm}^{-1}$), while the $V_{A'}$ surface was more repulsive and less anisotropic. Wagner *et al.* [43] presented an interesting discussion of model potentials for CH(X)+He. They noted that the traditional pair-potential model using nuclear centres alone could not represent the breaking of the orbital degeneracy that occurs for non-linear approach geometries. To incorporate this effect they proposed a model with three different terms for the C+He interaction to describe approach along the p_x, p_y and p_z orbitals of the C atom. This model successfully reproduced the main features of the *ab initio* potentials. Inelastic scattering calculations using the *ab initio* surfaces correctly predicted the observed propensities for population of levels of A'' and A' symmetry in upward and downward rotational energy transfer, respectively (for low values of j). The primary focus of the study by Wagner *et al.* [43] was on characterization of the repulsive regions of the CH(X)+He potentials. Cybulski *et al.* [45] revisited this problem using methods that were better suited to treatment of the long-range interactions. They used the UMP4 method as this could be used to decompose the van der Waals forces in terms of various contributing interactions. The well-tempered basis sets of Hunzinaga, augmented by f, d and mid-bond functions, were used. The qualitative properties of the surfaces of Cybulski *et al.* [45] were in agreement with the results of Wagner *et al.* [43]. As expected, the larger and more flexible basis set yielded deeper wells. The global minimum for the A'' surface was $D_e = 73.5\,\mathrm{cm}^{-1}$. Stationary point data for the potentials of Cybulski *et al.* [45] are given in table 3.

The interactions between CH(X) and Ne or Ar are sufficiently strong that the binary complexes are relatively easily formed at low temperatures. Multiphoton dissociation of Br_3CH has been used as the source of the radical in studies of the complexes. The A–X and B–X transitions of CH–Rg have been examined. Both excited states are derived from the $3\sigma 1\pi^2$ configuration. CH–Ar was first observed via the $B^2\Sigma^- – X^2\Pi$ transition. Lemire *et al.* [74] reported 12 bands of the complex associated with the monomer 0–0 transition, and 11 bands associated with 1–0. The rotational structures of eight bands were analysed. From these data, Lemire *et al.* [74] concluded that the

Table 3. Stationary point data for CH–Rg complexes.

Surface	D_e/cm^{-1}	θ_e	R_e/au	Reference
CH($X^2\Pi$)–He				
$V_{A'}$, *ab initio*	12	0	7.5	[45]
$V_{A'}$, *ab initio*	12	140	7.5	[45]
$V_{A''}$, *ab initio*	73.5	100	5	[45]
CH($X^2\Pi$)–Ne				
$V_{A'}$, *ab initio*	24	21	7.64	[58]
$V_{A'}$, *ab initio*	24	180	7.62	[58]
$V_{A''}$, *ab initio*	68	76.2	5.79	[58]
CH($A^2\Delta$)–Ne				
V, *ab initio*	43	0	7.11	[58]
V, *ab initio*	26	180	6.82	[58]
V, modified	65	0	6.64	[58]
V, modified	39	180	6.35	[58]
CH($B^2\Sigma$)–Ne				
V, *ab initio*	36	0	7.5	[78]
V, *ab initio*	29	180	7.26	[78]
CH($X^2\Pi$)–Ar				
$V_{A'}$, *ab initio*	60	51.5	7.65	[44]
$V_{A'}$, *ab initio*	60	180	7.76	[44]
$V_{A''}$, *ab initio*	212	83.5	5.85	[44]
$V_{A'}$, modified	78	53	7.41	[44]
$V_{A'}$, modified	76	180	7.56	[44]
$V_{A''}$, modified	268	84	5.64	[44]
CH($A^2\Delta$)–Ar				
V, *ab initio*	110.6	0	7.39	[57]
V, *ab initio*	75.9	180	6.99	[57]
V, modified	165.3	0	7.32	[57]
V, modified	141.8	180	7.2	[57]
CH($B^2\Sigma$)–Ar				
V, *ab initio*	133	0	7.33	[44]
V, *ab initio*	87	150	7.17	[44]
V, modified	180	0	7.06	[44]
V, modified	119	150.5	6.9	[44]

equilibrium geometry was bent for the ground state and linear for the B state. The rotational levels of the ground state resembled those of a molecule in a $^2\Sigma$ state with a modest spin–rotation splitting (i.e. levels primarily characterized by the integer quantum number N). All of the complex bands were blue-shifted relative to the monomer parent transitions. This, taken with the red-degraded rotational structures of the bands, indicated that the van der Waals bond was weakened and lengthened by electronic excitation. McQuaid *et al*. [75] reported a brief study of the CD–Ar bands associated with the monomer 1–0 transition. Overall the results were consistent with the observations for CH–Ar.

A detailed theoretical study of the CH–Ar B–X system was carried out by Alexander *et al*. [44]. Two-dimensional *ab initio* potential energy surfaces were calculated using MR–CI(D)/*avqz–f*+CP. The ground state potentials were qualitatively the same as those described above for CH(X)–He, but more deeply bound. The equilibrium

structure for the $V_{A''}$ surface of CH(X)–Ar was bent ($\theta_e = 83.5°$) with a well depth of 212 cm^{-1}. In contrast, the well depth of the $V_{A''}$ surface was 60 cm^{-1}. Promotion of a second electron into the $p\pi$ orbitals resulted in a potential energy surface for the B state where the global minimum ($D_e = 133\,cm^{-1}$) was for the linear CH–Ar complex. Stationary points for the potential energy surfaces of CH–Ar are listed in table 3. The *ab initio* calculations correctly predicted the equilibrium structures for the X and B state complexes and the weaker van der Waals bond for the electronically excited state. Modified potentials were used in bound state calculations, in order to obtain results that would be closer to the experimental data. The properties of the modified surfaces are also presented in table 3. An important point concerning the bound state calculations is that they were made with the assumption that the diatomic spin–orbit coupling constant for the ground state ($a_{SO} = 27.9\,cm^{-1}$) was not influenced by the interaction with the Ar atom. The bond energy of CH(X)–Ar was predicted to be $D_0 = 131.8\,cm^{-1}$, which was slightly lower than the experimental lower bound of $D_0 > 161\,cm^{-1}$. The rotational constant for the zero-point level calculated from the $\langle R^{-2} \rangle$ expectation value was $B_0 = 0.167\,cm^{-1}$, as compared to the measured value of $B_0 = 0.174(4)\,cm^{-1}$. Better agreement was obtained when the rotational constant was derived from the calculated results using the method applied to the experimental data. Fitting of the calculated energy levels for a range of J values to a rigid-rotor model yields an effective constant of $B_0 = 0.173\,cm^{-1}$. Furthermore, the rigid rotor model was clearly consistent with energy levels governed by the integer case (B) quantum number N. As for BH(A)–Ar, the most deeply bound states of CH(X)–Ar were consistent with motion on the $V_{A''}$ potential. Evidently the electrostatic splitting of the Π state orbital energies dominates over the spin–orbit interaction.

Lemire *et al.* [74] assigned the B state energy levels accessed by the lowest energy transitions as (0^0, 0), (1^0, 0), and (0^0, 1), where the labels are (n^K, v_c). The onset of bands with homogeneously broadened features provided a lower bound for the dissociation energy of $D_0 > 80\,cm^{-1}$. The dissociation energy and rotational constants predicted using the modified potential energy surface were in good agreement with experiment (e.g. $D_0(\text{calc}) = 88.5$, $B_0(\text{calc}) = 0.116$, $B_0(\text{exp}) = 0.113\,cm^{-1}$). The vibronic assignments of Lemire *et al.* [74] were confirmed and the (0^0, 2) band was identified. However, many of the observed bands remain unassigned, as unambiguous correlations between these features and the calculated energy levels could not be established. Alexander *et al.* [44] speculated that calculations based on a full three-dimensional potential energy surface may be needed to advance the interpretation of the B–X spectrum.

The $A^2\Delta$–$X^2\Pi$ transition of CH/D–Ar has been examined by Komissarov *et al.* [76] and Kerenskaya *et al.* [57]. The vibronic structure of the spectrum was dominated by progressions in the van der Waals stretch ($v_c = 0$–3) combined with excited bending levels. Seven bands of CH–Ar and five bands of CD–Ar were rotationally resolved and analysed. Like the B–X system, the A–X bands were blue-shifted relative to monomer with red-degraded rotational structure. Again this was indicative of a weaker van der Waals bond for the excited state. The rotational energy levels for CH/D–Ar were well represented by a rigid-rotor model with half-integer quantum numbers ($E_{ROT} = BJ(J+1)$). This was initially surprising, given the rather small spin–orbit coupling constant for CH(A) of $a_{SO} = -1.1\,cm^{-1}$. All levels of the monomer

conform to the Hund's case (b) limit. However, for CH(A)–Ar the rotational constants are $\leq 0.11\,\mathrm{cm}^{-1}$, yielding a ratio for a_{SO}/B above 9 which tends towards the case (A) coupling scheme of Dubernet *et al.* [46] (under the assumption that the spin–orbit interaction is unchanged by the van der Waals interaction).

Theoretical calculations were carried out to analyse the A state energy levels and develop realistic empirical potential energy surfaces. Two-dimensional *ab initio* surfaces were calculated using MR–CI(D)/*avqz*+CP. Contour plots of these surfaces are shown in figure 2 and the stationary point data are given in table 3. The $V_{A'}$ and $V_{A''}$ surfaces were found to be very similar. This was expected as the A' and A'' symmetry components of the Δ state correspond to $\pi_x\pi_{x'}$–$\pi_y\pi_{y'}$ and $\pi_x\pi_{y'}$–$\pi_y\pi_{x'}$ orbital occupations, both of which have cylindrically symmetric electron density distributions. The maximum difference between the surfaces, for a curve that followed the minimum energy path from $\theta = 0$ to 180°, was $8\,\mathrm{cm}^{-1}$, with $V_{A'} < V_{A''}$. This splitting cannot be explained by simple electrostatic considerations. The effect is quantum mechanical, having to do with the mixing of configurations through electron correlation. The accuracy of the repulsive region of these potentials was verified by Kind *et al.* [63], who used the *ab initio* results to model CH(A)+Ar collisional energy transfer data.

The energy level structure arising from the interaction of CH(A) with Ar is congested. Due to the small spin–orbit interaction, the $j = 3/5$ and 5/2 levels of $n = 2$ are close in energy for the free diatom. The interaction with a rare gas atom splits these levels into four and six P-states, respectively (where each 'state' is a pair of parity doublets). An approximate picture of the splittings for CH(A)–Ar is shown in figure 4, where interleaving of the manifolds arising from $j = 3/2$ and 5/2 is evident. In order to correlate this structure with the observed spectrum it was essential to determine which of these bending/hindered rotor states would be optically active. The transition was subject to the $\Delta P = 0, \pm 1$ selection rule. As the ground state has a well-defined value of $P = 1/2$, transitions to the $P = 5/2$ levels would not be observable. Explicit treatment of the transition intensities was required to make further progress with spectral

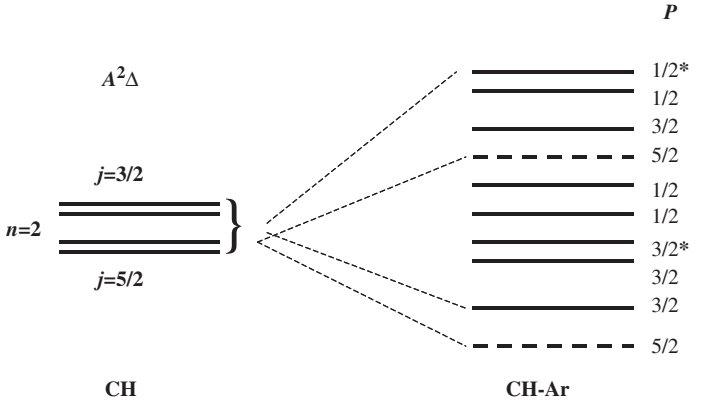

Figure 4. Energy level diagram showing the correlations between the lowest rotational levels of CH($A\,^2\Delta$) and the internal rotation levels of CH($A^2\Delta$)–Ar. The levels marked with asterisks are active in the A–X spectrum.

assignment. The first calculations used the modified CH(X)–Ar potential energy surfaces from ref. [44] and the *ab initio* surfaces for CH(A)–Ar. A spectral simulation derived from this calculation is compared with the experimental data in figure 5 (middle and upper traces, respectively), where it can be seen that the qualitative features of the spectrum were reproduced. However, the quantitative differences in the energy level spacings showed that the potentials were not sufficiently deep. An empirical form for the average potential was generated by adjusting the expansion coefficients of equation (4) to fit the observed energy level spacings. A key element of this process was the ability to track the relative intensities of the simulated spectrum as the potential was modified. The simulation for the optimized potential is shown in the lower trace of figure 5. The predicted energy level spacings were in good agreement with the experimental results for both CH(A)–Ar and CD(A)–Ar. The dissociation energy for CH(A)–Ar could not be estimated from the spectrum as the origin band was not observed. Instead, the data provided a lower bound for the binding energy for the first observed state of $>70\,\mathrm{cm}^{-1}$. The empirical potential yielded $72.4\,\mathrm{cm}^{-1}$ for this interval and a bond dissociation energy of $D_0 = 93.9\,\mathrm{cm}^{-1}$ for the $P = 5/2$ zero-point level. A satisfactory fit to the rotational constants was obtained by translating the potentials inward by 0.47 au. Stationary point data for the modified potentials are given in table 3.

The intensity distribution of the A–X spectrum was a matter of interest in its own right. Of the eight bending/hindered rotor states from $n = 2$ that could be accessed by ΔP allowed transitions, just two dominated the spectrum. Asterisks in figure 4 indicate the specific levels. The reason why the two lowest energy $P < 5/2$ states were not active in the spectrum could be seen by examining the angular probability distributions

$$D(\theta) = \int_0^\infty \left|\Psi(R,\theta)\right|^2 R^2 dR \tag{6}$$

where $\Psi(R,\theta)$ is an eigenfunction of equation 1. Angular probability distributions for states with $v_c = 0$, $J = 3/2$ are presented in figure 6. These plots show that the wavefunctions for the two lowest energy states (labelled 1 and 2) are located in the linear minima. As the ground state has a bent equilibrium geometry, the Franck–Condon overlap with these linear states is poor, resulting in weak transitions. The remaining distributions correspond to bent states, so it is not obvious from the $D(\theta)$ curves why the Ψ_3 and Ψ_8 states are particularly favoured. This preference is determined by the phase relationships among the basis set expansion coefficients.

The isotope shift for CH/D–Ar is a second point of interest. The lowest energy bands of the A–X system are blue-shifted, relative to the monomer transitions, by $98\,\mathrm{cm}^{-1}$ (CH–Ar) and $122\,\mathrm{cm}^{-1}$ (CD–Ar). The calculations predict an isotope shift of $2\,\mathrm{cm}^{-1}$ for the upper state level involved, which implies that the ground state zero-point energies must differ by $26\,\mathrm{cm}^{-1}$. Calculation of the ground state isotope shift using the potentials of Alexander *et al.* [44] gives $17\,\mathrm{cm}^{-1}$. This relatively large isotope effect is a consequence of the strongly anisotropic $V_{A''}$ potential energy surface. The discrepancy between the experimental and calculated shift is probably due to a combination of errors in the depth and anisotropy of the ground state potentials.

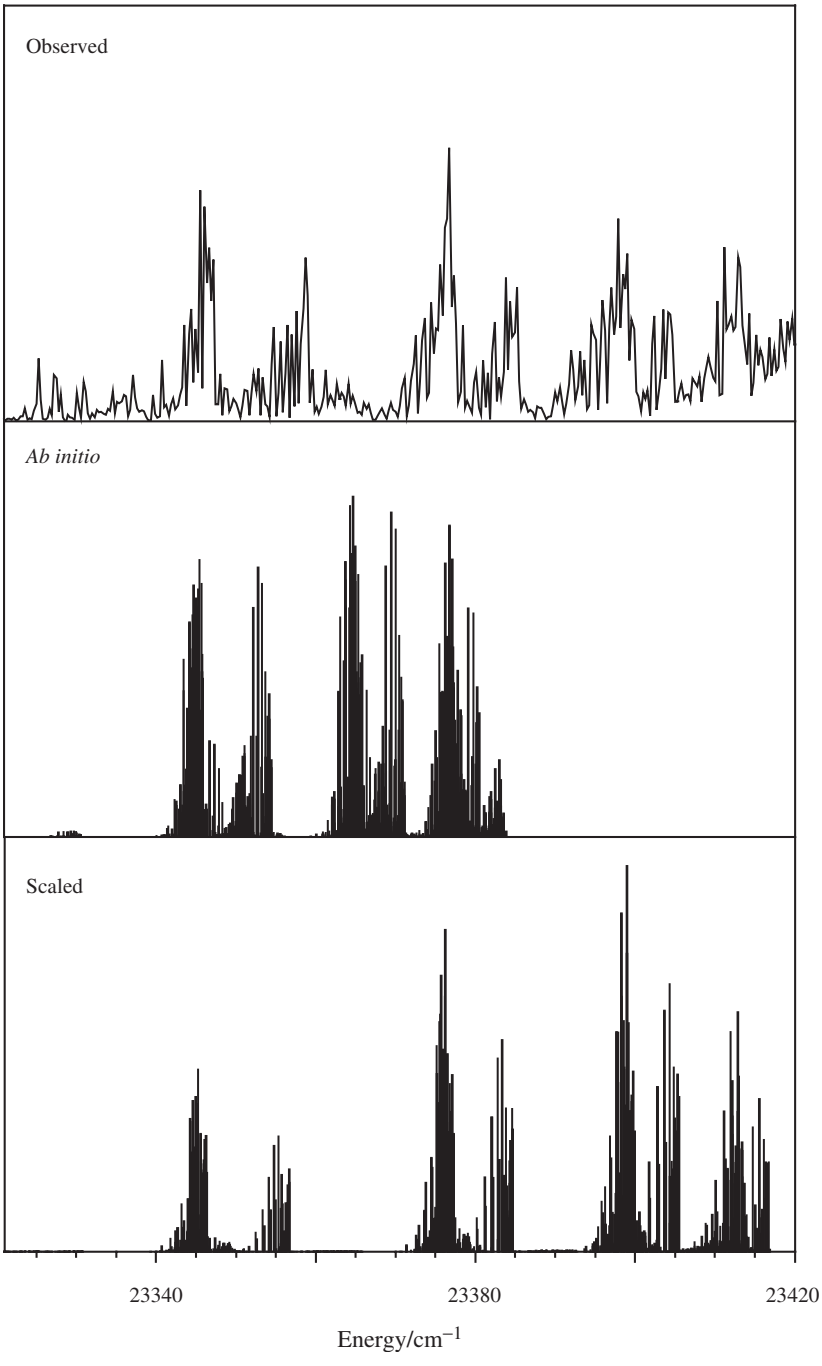

Figure 5. Comparison of experimental and simulated spectra for the $A^2\Delta$–$X^2\Pi$ transition of CH–Ar. Upper trace: low-resolution experimental spectrum from reference [76]; middle trace: simulated spectrum generated from the *ab initio* potential energy surfaces ($T = 4.0$K); lower trace: simulated spectrum generated from the adjusted potential energy surfaces of reference [57].

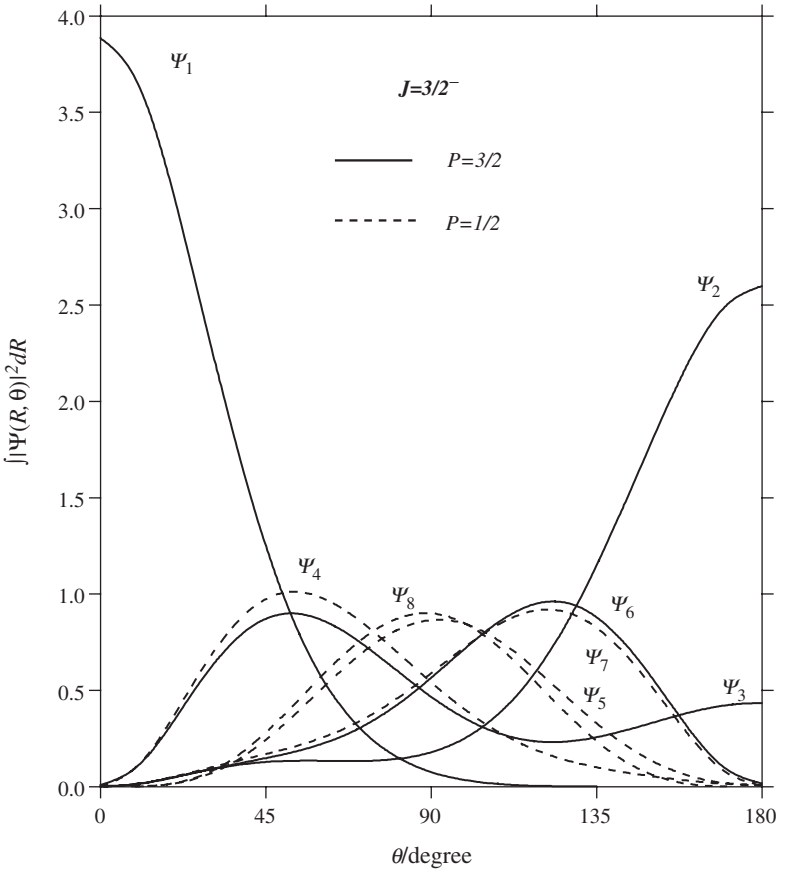

Figure 6. Angular probability distributions for CH($A^2\Delta$, $n=2$)–Ar. This plot shows the data for the eight lowest energy levels with $J=1.5^-$.

Studies of the B–X system of CH/D–Ne were carried out by Basinger *et al.* [77]. The ro-vibrational structure of CH(B)–Ne clearly reflected the nearly free internal rotation of CH within the complex. Transitions to levels with $n=0$, 1, and 2 were readily identified. Figure 7 shows the observed transitions for $v_c=0$, and their relationship to the transitions of free CH. The B state potential was just deep enough to support one bound level with $v_c=1$ ($n=0$, $K=0$). The $K=0$ and 1 components of $n=1$ were both above the dissociation asymptote, and the $K=0$ rotational levels were measurably broadened by rotational predissociation. Features associated with $n=2$ were also homogeneously broadened. Fluorescence depletion (FD) measurements were used to demonstrate that the $n=0$ and 2 levels of the complex were accessed from the ground state zero-point level, while the $n=1$ states were accessed from an excited level of the ground state. As indicated in figure 7, this was due to the diatomic parity being largely conserved in the complex. The separation of the ground state $P=1/2^+$ and $1/2^-$ pair was estimated to be $5\,\mathrm{cm}^{-1}$. Rotational constants of $B_0(1/2^+)=0.177$ and $B_0(1/2^-)=0.167\,\mathrm{cm}^{-1}$ were determined. Due to the high laser power used to record the

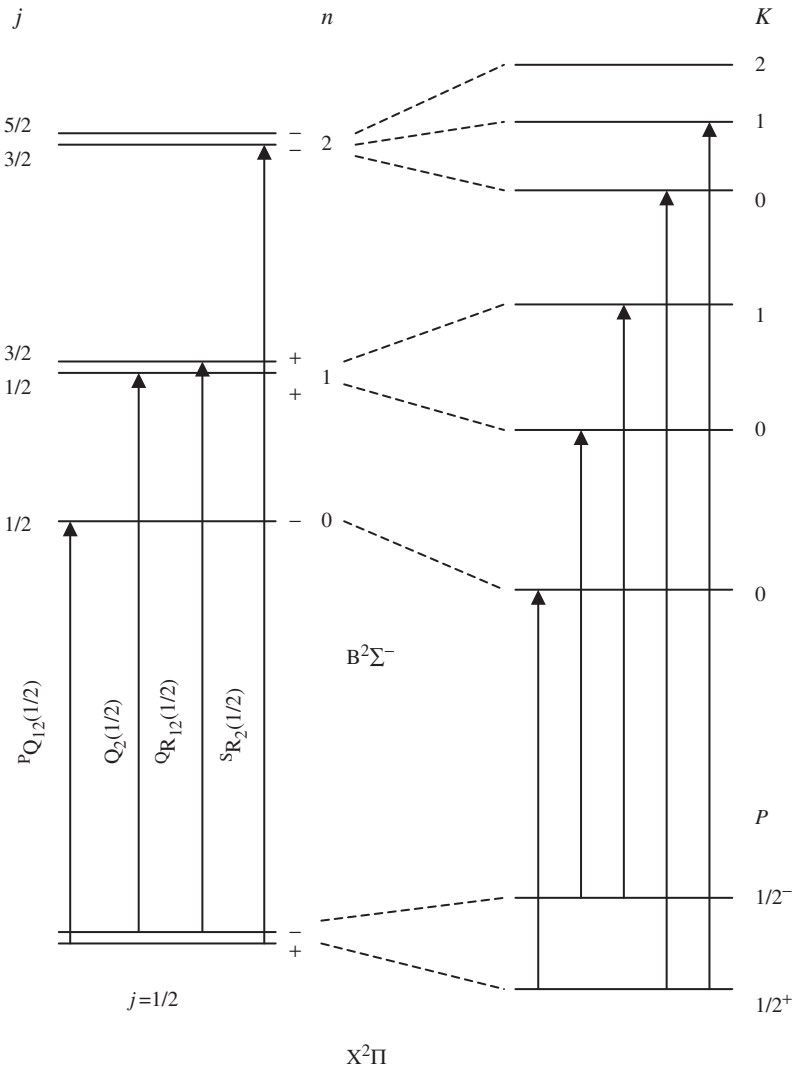

Figure 7. Schematic diagram showing the relationship between the allowed rotational transitions of CH *B*–*X* and the prominent hindered internal rotation bands seen in the spectrum of CH–Ne.

FD spectrum, transitions to the CH(*B*)+Ne continuum were observed. The onset of the continuum, combined with the frequencies for the origin band and the monomer $^{P}Q_{12}(1/2)$ line, defined bond energies of $D_0 = 26.3(4)$ and $D_0 = 19.6(3)$ cm^{-1} for $v = 0$ CH(*B*). The energy level structure observed for CH(*B*, $v = 1$)–Ne was very similar to that for $v = 0$, the only difference being that the van der Waals bond was slightly weakened by CH vibrational excitation ($D_0(v = 1) = 18.8(5)$ cm^{-1}).

The rotational structure of the CH–Ne bands was significantly different from that of the CH–Ar bands. For example, the origin band for CH–Ar exhibited the

characteristics of a $^2\Sigma$–$^2\Sigma$ transition, while that of CH–Ne was consistent with $^2\Sigma$–$^2\Pi$ line-strengths. The rotational energy levels of the ground state were governed by half-integer rotational quantum numbers. These observations seem to suggest a linear geometry for CH(X)–Ne, but theoretical calculations show that the equilibrium geometry is bent.

Ab initio potential energy surfaces for CH–Ne were generated for the ground state and the excited states derived from the $3\sigma 1\pi^2$ configuration ($X^2\Pi$, $A^2\Delta$, $B^2\Sigma^-$ and $C^2\Sigma^+$) (state-averaged CASSCF, MRCI/ *avqz*+CP [58]). Stationary point data for the X, A and B state surfaces are listed in table 3. Bound state calculations for the X state were carried out for the unmodified potentials. These predicted a bond dissociation energy of 15.5 cm^{-1}, a $P = 1/2^+$ to $1/2^-$ interval of 1.4 cm^{-1} and rotational constants $B_0(1/2^+) = 0.142$, $B_0(1/2^-) = 0.136$ cm^{-1}. Qualitative details such as $E(1/2^+) < E(1/2^-)$, $B_0(1/2^+) > B_0(1/2^-)$ and the case A angular momentum coupling were correctly reproduced. The quantitative discrepancies indicated that the well depths of the potential surfaces needed to be increased by a factor of approximately 1.7 and the surfaces should be translated inward along R by 0.7 au. Bound state calculations for the B state potential have not been carried out, but the quantitative details of the surface are in agreement with the spectroscopic data (linear equilibrium geometry with V_{20} as the dominant component of the surface anisotropy). Note also that the *ab initio* calculations correctly predicted that $D_e(B) < D_e(X, A'')$.

The A–X system of CH–Ne was particularly congested and difficult to analyse. LIF spectra recorded at a resolution of 0.06 cm^{-1} could not be assigned using the conventional combination differences approach. FD techniques were applied in order to obtain interpretable data. For these experiments a probe laser was fixed on an assigned rotational line of the B–X system. The depletion laser was then tuned through A–X bands, inducing a drop in the B–X fluorescence intensity whenever a transition from the probe-selected lower level was encountered. By this means the transitions from a single rotational level of the ground state could be isolated. An example of the FD spectrum connected with the $J = 1/2$ level of the ground state is shown in figure 8. FD spectra were recorded for all J levels in the range from 1/2 to 9/2. Transitions to the eight states from $n = 2$ with $P = 1/2$ and 3/2 were identified. This was responsible for the complexity of the spectrum and contrasted with the situation for CH(A)–Ar, where only two of these states were optically active. The stick spectrum in the centre of figure 8 (trace b) shows the energy levels predicted from the *ab initio* potentials. The qualitative energy level pattern predicted by the calculations was correct, and the energy ordering of the hindered rotor states was the same as that shown in figure 4 for CH(A)–Ar. Clearly the spacings of the predicted bands (figure 8b) were underestimated, indicating the usual problem with underestimation of the well depth. To fit the experimental data the average potential energy surface was modified by increasing the V_{00} and V_{20} terms of equation (4) by a factor of 1.5. The stick spectrum from the adjusted potential, shown as trace c in figure 8, was in excellent agreement with the observed band structures. The angular probability distributions for the wavefunctions of the modified potential were similar to those shown in figure 6 for CH(A)–Ar, but more delocalized. The probability distributions for the ground state provided the key to understanding the different intensity distributions of CH–Ne versus CH–Ar A–X band systems. The ground state wavefunction for CH(X)–Ne is far

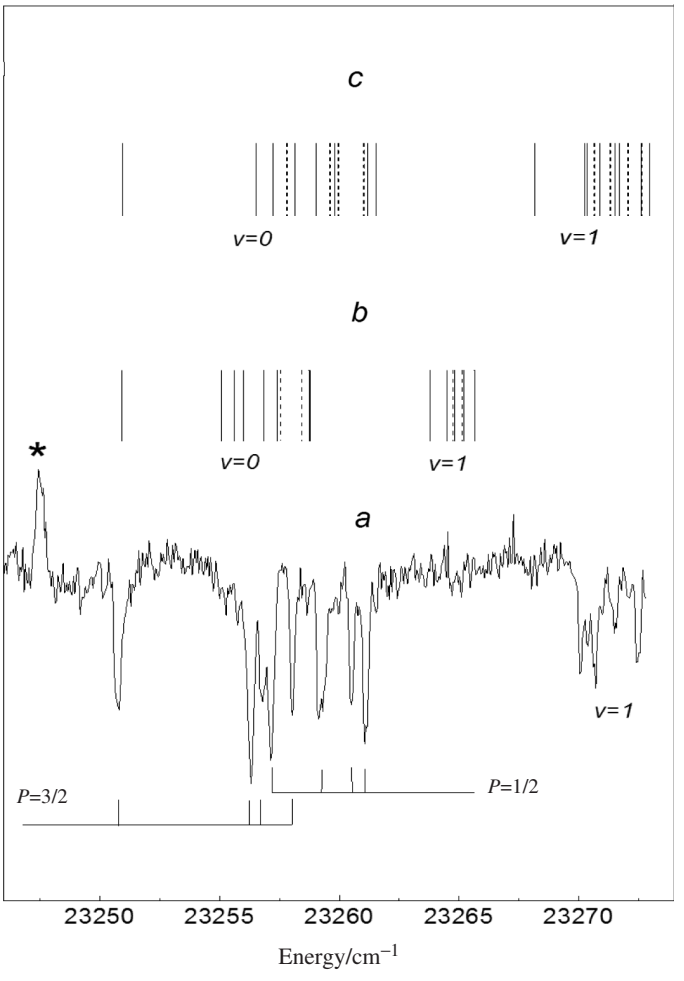

Figure 8. Comparisons of theoretically predicted energy level patterns with the fluorescence depletion spectrum obtained by monitoring transitions from the $J=1/2_e$ rotational level of the ground state. The calculated positions of the R and Q lines are given by solid and broken lines. Stick spectra (b) and (c) were obtained using *ab initio* and scaled potential energy surfaces, respectively. *P*-assignments for the observed transitions are given below the experimental spectrum (trace a).

more delocalized than that of CH(X)–Ar, permitting favourable overlap with the wavefunctions for all levels of CH(A)–Ne ($v_c=0$) that could be accessed by ΔP allowed transitions. The probability distribution plots for CH(A)–Ne also explain why the lowest energy bright state ($P=3/2$ near 23 250 cm^{-1} in figure 8) stands apart from the remainder of the $v_c=0$ hindered rotor levels. This state, and the lowest energy $P=5/2$ state, are localized near the global minimum of the potential. All other states are delocalized to the extent that they have appreciable probability densities in the region of the barrier that separates the two linear minima. The binding energy of the lowest $P=3/2$ state was predicted to be 23.1 cm^{-1} in agreement with the measured value of 23.0 cm^{-1}.

Inward translation of the scaled potential energy surfaces by 0.47 au yielded agreement between the observed and calculated rotational constants [58]. In comparing the results it was important to include the effects of Coriolis coupling, as the various *P*-states were not widely separated. There was a marked difference between constants obtained from $\langle R^{-2} \rangle$ expectation values and those derived by fitting to *J*-dependent energies. For example, the measured constant for the highest energy $P = 1/2$ ($v_c = 0$) state was $0.185\,\mathrm{cm}^{-1}$. The values calculated from $\langle R^{-2} \rangle$ and energy level fitting were 0.125 and $0.185\,\mathrm{cm}^{-1}$, respectively.

Comparing the properties of CH(*A*)–Rg and CH(*B*)–Rg complexes it is apparent that, for a given Rg, the potential energy surfaces are very similar for the two electronic states. This supports the notion that the shapes and depths of the potentials are primarily governed by the orbital occupation. In this context it is worth noting that the *ab initio* potential energy surface for CH($C^2\Sigma^+$)–Ne is also very similar to the surfaces of the *A* and *B* states [78]. When the properties of CH–Rg complexes are compared with those of other open-shell Rg–HX systems there is one curious anomaly. Electronic excitation of CH–Rg weakens the van der Waals bond while BH–Rg, NH–Rg and OH–Rg complexes all show the opposite trend. *Ab initio* calculations successfully predict shallower potentials for the $3\sigma 1\pi^2$ excited states of CH–Rg, but the origin of the effect is not obvious. Decomposition of the CH–Rg excited state interactions into components such as dispersion, dipole–induced-dipole and exchange repulsion should provide insights concerning this behaviour.

4.3. *NH–Rg complexes (Rg = He, Ne and Ar)*

NH–Rg complexes provide another opportunity for studies of the van der Waals interactions involving multiple electronic states that are derived from a common electronic configuration, with the additional dimension of allowing comparisons of the properties of states with triplet and singlet spin multiplicity. The ground and low-lying electronic states of NH, $X^3\Sigma^-$, $a^1\Sigma$ and $b^1\Sigma^+$, are derived from the $3\sigma^2 1\pi^2$ configuration. The excited states that are readily observed by LIF are $A^3\Pi$ and $c^1\Pi$, derived from the $3\sigma 1\pi^3$ configuration. Potential energy surfaces for several NH–Rg systems have been reported. One of the earliest high-level theoretical studies was carried out by Jansen and Hess [79], who mapped the surfaces for the *X*, *a*, and *b* states of NH–Ar. They used CASSCF calculations, combined with an average coupled-pair functional treatment of electron correlation. Counterpoise and self-consistency corrections were applied. With a filled 3σ orbital and two $p\pi$ electrons the NH(*X*)–Ar potential energy surface was found to have a rather low barrier to internal rotation, with a bent equilibrium structure ($\theta_e = 63^\circ$, $D_e = 75\,\mathrm{cm}^{-1}$). The potential energy surfaces for the *a* and *b* states had minima for the linear configurations, with the same general properties as the CH(*A*)–Ne surfaces shown in figure 2. The dissociation energies were $D_e(a) = 80$ and $D_e(b) = 85\,\mathrm{cm}^{-1}$. For the reasons discussed above for CH(*A*)–Rg, the difference potential for NH(*a*)–Ar was much smaller than the average potential. The dominant isotropic component of the interaction energy ($V_{00}(R)$) was comparable for all three electronic states. More recently, Kendall *et al.* [80] used UMP4 calculations with large basis sets (*avtz* and *WTdf*, both augmented with mid-bond functions) to generate a more accurate surface

for NH(X)–Ar. Their surface was similar to that of Jansen and Hess [79], but more deeply bound ($D_e = 100.3\,\mathrm{cm}^{-1}$). Stationary point data for the potential energy surfaces of NH–Ar are collected in table 4. Kendall *et al.* [80] used the diffusion Monte Carlo technique to predict the properties of the NH(X)–Ar zero-point level. This yielded a bond energy of $D_0 = 71.5\,\mathrm{cm}^{-1}$ and an angular probability distribution that indicated nearly free internal rotation of NH(X).

To date, there are no experimental data for the NH(X)–Ar complex. In part this is due to the fact that most photolytic sources of NH have high branching fractions for production of the radical in the metastable $a^1\Delta$ state. Consequently, Randall *et al.* [81] observed the c–a band system of NH–Ar using 193 nm photolysis of HNCO to generate NH(a). Fourteen bands of the complex were observed in association with the monomer 0–0 transition. The lowest energy bands were red-shifted, indicating a stronger van der Waals bond for the excited state. A full theoretical treatment of the spectrum was required before the vibronic structure could be assigned. Yang *et al.* [53] calculated the potential energy surfaces for NH(c)–Ar at the MRCI(D)/*avqz* level of theory, including the CP corrections. Consistent with the $3\sigma 1\pi^3$ orbital occupation, the surfaces had minima for the linear geometries, with a dissociation energy of $D_e = 361\,\mathrm{cm}^{-1}$. The difference potential for NH(c)–Ar was significant, but not nearly as large as the difference potentials of BH($A^1\Pi$)–Ar or CH($X^2\Pi$)–Ar. This was expected, as the charge distribution for π^3 is more symmetrical than that for a singly occupied $p\pi$ electron. Prior to prediction of the NH–Ar c–a spectrum, Yang *et al.* [53] scaled and shifted the *ab initio* potentials (see table 4 for details of the modified potentials). Bound state calculations for NH(a)–Ar produced manifolds of closely spaced levels. The $j = 2$ level of the monomer gives rise to states with $P = 2_l$, 0^+, 1_l, 0^-, 1_u, and 2_u, with the first three states separated by just $4.1\,\mathrm{cm}^{-1}$. This congested structure was the result of the weak anisotropy of the NH(a)–Ar potentials. The bound levels of NH(c)–Ar correlate with the monomer $j = 1$ and 2 levels. The former correlates with the $P = 1_l$, 0^+, 1_u, and 0^- states of the complex. Yang *et al.* [53] noted that the adiabatic bender potentials for the 0^+ and 0^- states were equivalent to motions on the $V_{A'}$ and $V_{A''}$ surfaces, respectively. This was similar to the situation encountered for BH($A^1\Pi$)–Ar, but the energy ordering of the states was inverted as the $V_{A'}$ surface is more attractive for the π^3 orbital occupation. The adiabatic bender curves for the $P = 1_l$ and 1_u states were indicative of motions that sampled both potentials. Using the calculated results, Yang *et al.* [53] were able to provide vibronic assignments for eleven bands of the c–a system. Rotational analyses of three of these bands provided clear evidence that transitions from the $P'' = 2_l$, 1_l and 0^+ states contributed to the spectrum. The Coriolis coupling between these bands was examined using a perturbation theory approach. To reproduce the observed state rotational energy level pattern, Yang *et al.* [53] found that they had to decrease the energy spacings between the 2_l, 1_l and 0^+ states, which implied that the true potential energy surfaces are even less anisotropic than the theoretical surfaces. Comparing the calculated dissociation energies ($D_0(a) = 95$, $D_0(c) = 292\,\mathrm{cm}^{-1}$) with the experimental lower bounds ($D_0(a) > 127$, $D_0(c) > 309\,\mathrm{cm}^{-1}$), they concluded that further deepening of the modified potentials would be justified.

Theoretical and experimental studies of the c–a system of NH/D–Ne were carried out by Kerenskaya *et al.* [82]. One of the issues investigated in this work was the validity

Table 4. Stationary point data for NH–Rg complexes.

Surface	D_e/cm^{-1}	θ_e	R_e/au	Reference
NH($X^3\Sigma$)–He				
V, *ab initio*	19.84	62.3	6.33	[15]
NH($A^3\Pi$)–He				
V_{ave}, *ab initio*	36	0	6.24	[84]
V_{ave}, *ab initio*	25	180	5.67	[84]
NH($X^3\Sigma$)–Ne				
V, *ab initio*	42.3	63.7	6.46	[83]
NH($a^1\Delta$)–Ne				
V_{ave}, *ab initio*	43	0	7.41	[82]
V_{ave}, *ab initio*	28	180	6.80	[82]
NH($A^3\Pi$)–Ne				
V, *ab initio*	95	0	6.41	[83]
V, *ab initio*	47	180	6.00	[83]
vi) NH($c^1\Pi$)–Ne				
V_{ave}, *ab initio*	97	0	6.46	[82]
V_{ave}, *ab initio*	42	180	6.10	[82]
NH($X^3\Sigma$)–Ar				
V, *ab initio*	100.3	67	6.75	[80]
NH($a^1\Delta$)–Ar				
V, *ab initio*	80	0	7.66	[79]
V, *ab initio*	68	180	7.24	[79]
V, modified	124	0	7.27	[53]
V, modified	105	180	6.88	[53]
NH($c^1\Pi$)–Ar				
V_{ave}, *ab initio*	361	0	6.18	[53]
V_{ave}, *ab initio*	129	180	6.16	[53]
V_{ave}, modified	541	0	5.76	[53]
V_{ave}, modified	287	180	5.86	[53]

of the CP correction that has been routinely applied in the calculation of potential energy surfaces for open-shell van der Waals complexes. Experience shows that the typical calculations described above (e.g. MRCI with an *avtz* or *avqz* basis set) will overestimate the binding energies and underestimate the R_e values due to the basis set superposition error. Application of the full CP correction then appears to over-compensate. Calculations for NH–Ne can be performed using a near-saturated basis set, where the CP correction should tend to zero. Kerenskaya *et al.* [82, 83] explored the approach to this limit by calculating potentials for the *X*, *a*, *A* and *c* states using basis sets that ranged in size from *avdz* to *av*6*z*. Three different correlation methods, CASPT2, CASPT3 and MRCI, were tested. Trial calculations showed that CASPT2 yielded results that were comparable to CASPT3 and MRCI, and therefore provided the best compromise between computational expense and accuracy. Linear NH–Ne equilibrium geometries were predicted for the singlet states (*a* and *c*) for all of the basis sets investigated. The effect of increasing the basis set size was conveniently followed by tracking the D_e and R_e values. These data are presented in figure 9, which shows results computed with and without the CP correction. Overall these plots show the

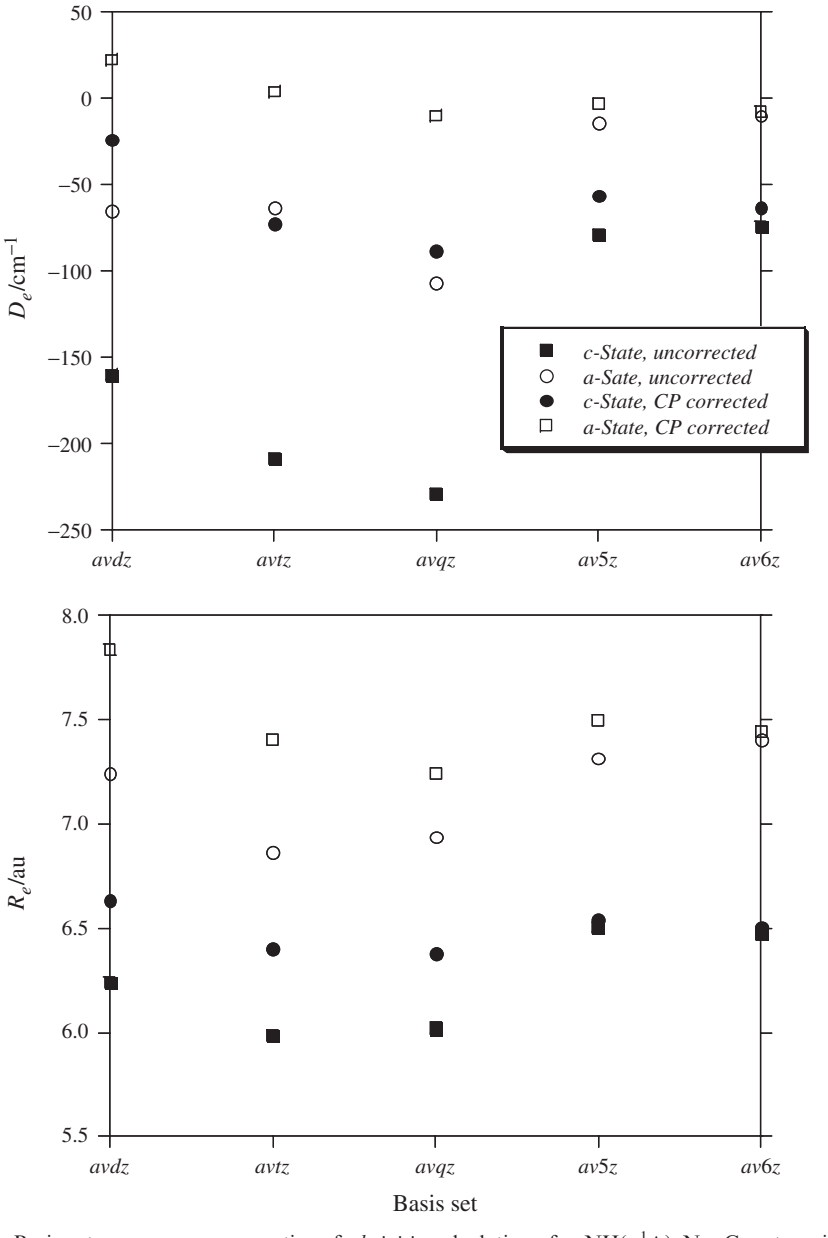

Figure 9. Basis set convergence properties of *ab initio* calculations for NH($a^1\Delta$)–Ne. Counterpoise (CP) corrected and uncorrected binding energies and equilibrium distances, computed with truncated *avdz* to *av6z* basis sets.

anticipated trends. The uncorrected D_e values were always larger than the CP corrected values, and the two appeared to converge for the largest basis set. Similarly, the uncorrected R_e values converged towards the CP corrected values. Note also that the CP correction worked well for the smaller basis set calculations. A surprising aspect

of figure 9 was the rather erratic shape of the D_e and R_e curves, which precluded asymptotic extrapolation of the results to the complete basis set limit. Similarly erratic trends have been observed in attempts to perform basis set extrapolations for Ne–HF and Ar–HF [59].

Two-dimensional potential energy surfaces for the X, a, A and c states were calculated using the CASPT2/*av6z* combination without the CP correction (stationary point data given in table 4). Contour diagrams for the A'' surfaces of the singlet states are shown in figure 10. The effect of electronic excitation on the well depth and anisotropy of the van der Waals interaction is readily apparent here. Bound state calculations were used to predict the characteristics of the c–a band system. The stable states of NH(a)–Ne, $P = 2_l$, 0^+, 1_l, 0^-, 1_u, and 2_u, correlate with $j = 2$. Due to the nearly isotropic potential energy surface, the zero-point levels for these six states fell within a $7\,\mathrm{cm}^{-1}$ energy interval. Based on these results it was expected that two or three of the lowest energy P states would be populated under the conditions typically used to observe Rg–HX complexes. Calculated values for the bond energy and rotational constant were $D_0 = 20.4\,\mathrm{cm}^{-1}$ and $B_0 = 0.111\,\mathrm{cm}^{-1}$ (including the Coriolis effect).

Adiabatic bender curves for NH(c)–Ne are shown in figure 11, where the stable bound states correlate with $j = 1$ ($P = 1_l$, 0^+, 1_u, 0^-). States correlating with $j > 1$ were unstable with respect to rotational predissociation. As compared to NH(a)–Ne, the P states of NH(c)–Ne were more widely separated due to the greater anisotropy of the excited state surfaces. Consequently, the rotational energy levels were less influenced by Coriolis coupling than those of the a state. Calculated values for the binding energy and zero-point rotational constant ($P = 1_l$) were $D_0 = 29.6$ and $B_0 = 0.147\,\mathrm{cm}^{-1}$. The large zero-point energy for NH(c)–Ne of $67\,\mathrm{cm}^{-1}$, which is 2/3 of the well depth, resulted from the steep rise of the potential in the vicinity of the global minimum. The energy of the zero-point level is close to the barrier to internal rotation at $70\,\mathrm{cm}^{-1}$, so NH(c) is essentially a free rotor for all bound states. Calculations for the a and c states of ND–Ne yielded bound state predictions that were not much different from those obtained for NH–Ne. For example, deuteration increased the binding energy for the c state by just $2.6\,\mathrm{cm}^{-1}$.

Experimental studies of NH/D–Ne utilized photolysis of both HNCO and NH_3 to generate NH(a). Photolysis of ND_3 was used to obtain ND(a). Spectra were recorded in the vicinity of the monomer c–a 0–0 transition [82]. In accordance with the theoretical prediction, the rotational levels of the monomer were reflected in the spectrum of the complex. Bands of NH–Ne were observed in association with the monomer P(2), Q(2) and R(2) lines. As the bands associated with Q(2) and R(2) were broadened by predissociation, the focus of the spectroscopic work to date has been on the stable states associated with $j = 1$. These formed a compact group of at least twelve bands contained within a $45\,\mathrm{cm}^{-1}$ interval. Partial rotational resolution was achieved for six features. Band contour analyses indicated that transitions from the $P = 2_l$ and 1_l states contributed to the spectrum. Comparisons with the theoretical results were used to propose assignments for the seven lowest energy bands. Lower bounds for the binding energies of $D_0(a) > 19.8$ and $D_0(c) > 42.4$ were established. Surprisingly, the rotational constants derived from the experimental data were smaller than the calculated values. Scaling of the latter by factors of 0.8 (a) and 0.7 (c) yielded respectable simulations of the rotational band contours.

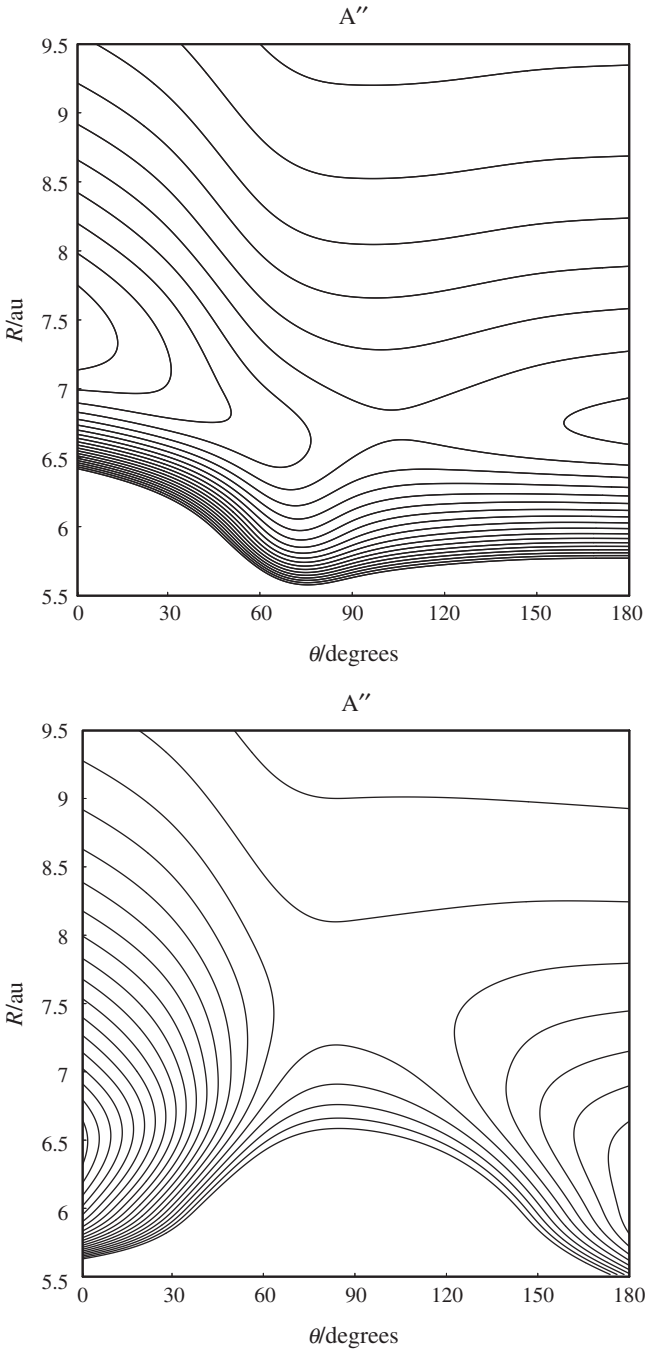

Figure 10. Contour plots of the potential energy surfaces for NH–Ne. The upper panel shows the A'' surface for NH($a^1\Delta$)–Ne. The contours are drawn from the linear NH–Ne geometry contour at $-41\,\mathrm{cm}^{-1}$ with $4\,\mathrm{cm}^{-1}$ intervals. The lower panel shows the A'' potential energy surface for NH($c^1\Pi$)–Ne. The contours are drawn from the linear NH–Ne geometry contour at $-94\,\mathrm{cm}^{-1}$ with $6\,\mathrm{cm}^{-1}$ intervals.

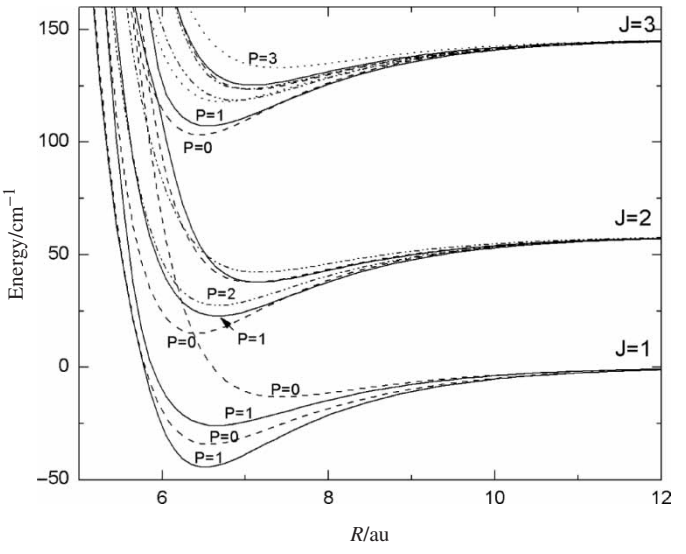

Figure 11. Adiabatic bender potentials for NH($c^1\Pi$)–Ne for an effective angular momentum of $L=1$. For clarity the dashed curves correspond to $P=0$ and the solid curves to $P=1$.

The experimental data for NH–Ne indicated that the errors in the *ab initio* potential energy surfaces for the *a* state were relatively small. The dissociation energy was in good agreement with the experimental lower bound. Calculated rotational constants for the $P=2_l$ and 1_l levels of $j=2$ were appreciably larger than the constants derived from the band contour models. However, this does not necessarily imply that the R_e value had been underestimated. These constants are strongly influenced by Coriolis mixing with the other low-lying states. Reducing the splitting between the various $j=2$ states would bring the effective constants into agreement with the results of the contour analyses. This points to possible errors in the anisotropy of the surfaces. The discrepancies for the *c* state surfaces were more significant and somewhat unusual. The measured upper bound for the dissociation energy was greater than the calculated value by a factor of 1.4. As this is too large to be a zero-point effect it shows that the theoretical potentials were too shallow. Contrary to the usual trend, the rotational constants were overestimated. This could not be accounted for by Coriolis effects and clearly indicated that the theoretical potentials needed to be translated out along the *R* axis by 0.4 au. Despite these discrepancies, the theoretical results for the singlet states of NH–Ne indicated that the CP correction was not the source of the errors. The calculations for NH(X)–Ne described below indicate that part of the problem comes from incomplete recovery of the correlation energy. Recent calculations also show that improved results are obtained when the basis sets are augmented by the inclusion of mid-bond functions.

Spectra for the $A^3\Pi$–$X^3\Sigma^-$ transition of NH–Rg (Rg = He, Ne) provided the first experimental data for complexes involving a radical in a $^3\Pi$ state [83, 84]. The rotation and spin–orbit coupling constants for NH(A), $v=0$, are $b=16.32$ and $a_{SO}=-34.6\,cm^{-1}$. The low rotational levels are intermediate between Hund's coupling cases (a) and (b), but close enough to case (a) that ω is a useful quantum number.

Following the usual convention, the three spin components are labelled F_1, F_2, and F_3, and for low values of j these are approximately $^3\Pi_2$, $^3\Pi_1$ and $^3\Pi_0$. For example, the F_1, $j=2$ level is given, in terms of pure case (a) basis functions, by the superposition $0.899|^3\Pi_2\rangle - 0.412|^3\Pi_1\rangle - 0.150|^3\Pi_0\rangle$. Note that the energy ordering is $\omega = 2 < 1 < 0$ as the spin–orbit coupling constant is negative. NH/D(X)–Ne was produced using photolysis of NH_3/ND_3 as the radical source. Under jet-cooled conditions the A–X, 0–0 band of the monomer shows three strong rotational lines originating from the X state $n=0$, $j=1$ level. These are the $R_{11}(1)$, $Q_{21}(1)$ and $P_{31}(1)$ lines which terminate on the upper state F_1, $j=2$, F_2, $j=1$ and F_3, $j=0$ levels, respectively. Bands of the NH/D–Ne complex were observed in groups around these rotational lines. This pattern indicated that the ro-vibronic structure of NH(A) was mostly preserved in the complex (e.g. nearly free internal rotation with no apparent quenching of the spin–orbit coupling). Sharp rotational structure was observed for two complex features that were close to the monomer $R_{11}(1)$ line (bands 1 and 2) and one band associated with $Q_{21}(1)$ (band 3). The rotational structures of bands 1 and 3 were well resolved and readily assigned to $P'=2$–$P''=1$ and $P'=0^-$–$P''=0^-$ transitions, respectively. The spin splitting of the $^3\Sigma^-$ ground state was not resolved. Band 2 was a congested overlapping of at least four vibronic transitions. On close examination of band 3 it could be seen that the lines were perceptibly broadened by predissociation. The complex features above the $Q_{21}(1)$ line did not show resolvable structure due to rapid predissociation. Upper bounds for the bond energies of $D_0(A) < 40.4$ and $D_0(X) < 28.0\,\mathrm{cm}^{-1}$ were based on the onset of predissociation.

The CASPT2/*av6z* calculations for NH(X)–Ne predicted a linear equilibrium geometry [83], which was suspicious, as the highest level calculations for NH(X)–Ar [80] and NH(X)–He [15] predicted bent equilibrium structures. The CASPT2/*av6z* surface was weakly anisotropic, such that small errors could have a dramatic effect on the angular location of the minimum. To test the robustness of this result, further calculations were carried out using the more accurate RCCSD(T) method [83]. For all basis sets larger than *avdz* this method predicted a bent equilibrium geometry, with a Jacobi angle near 60°. Additional improvements were achieved by adding mid-bond functions to the basis set (RCCSD(T)/*av6z*–BF+CP). Compared to the CASPT2/*av6z* results, RCCSD(T)/*av6z*–BF+CP did not change the well depth significantly, but the equilibrium angle shifted to 63.7° and the R_e value contracted from 7.36 to 6.46 au. Bound state calculations for the RCCSD(T)/*av6z*–BF+CP potential predicted a bond energy of $D_0(X) = 23.5\,\mathrm{cm}^{-1}$ and rotational energy levels that were governed by the end-over-end rotational quantum number L. The spin splitting was of the order of $0.01\,\mathrm{cm}^{-1}$, which is well below the resolution of the available spectra. The calculated bond energy was within the experimental upper bound, and the rotational constant, $B_0 = 0.147\,\mathrm{cm}^{-1}$, was on the edge of the error range for the measured constant $B_0 = 0.149(2)\,\mathrm{cm}^{-1}$.

Energy levels for NH(A)–Ne were calculated using the CASPT2/*av6z* surfaces. Adiabatic bender curves for states correlating with the lowest energy levels of NH(A) are shown in figure 12. Bands 1, 2 and 3 of the A–X spectrum could be assigned by inspection of this figure. Band 1 terminated on the well-separated $P'=2_l$, F_1 state while the closely spaced $P'=1_l$, 0^-, 2_u and 1_u states were responsible for the congested structure of band 2. Band 3 is assigned to the $P'=0^-$, $j=1$, F_2 level, which, consistent

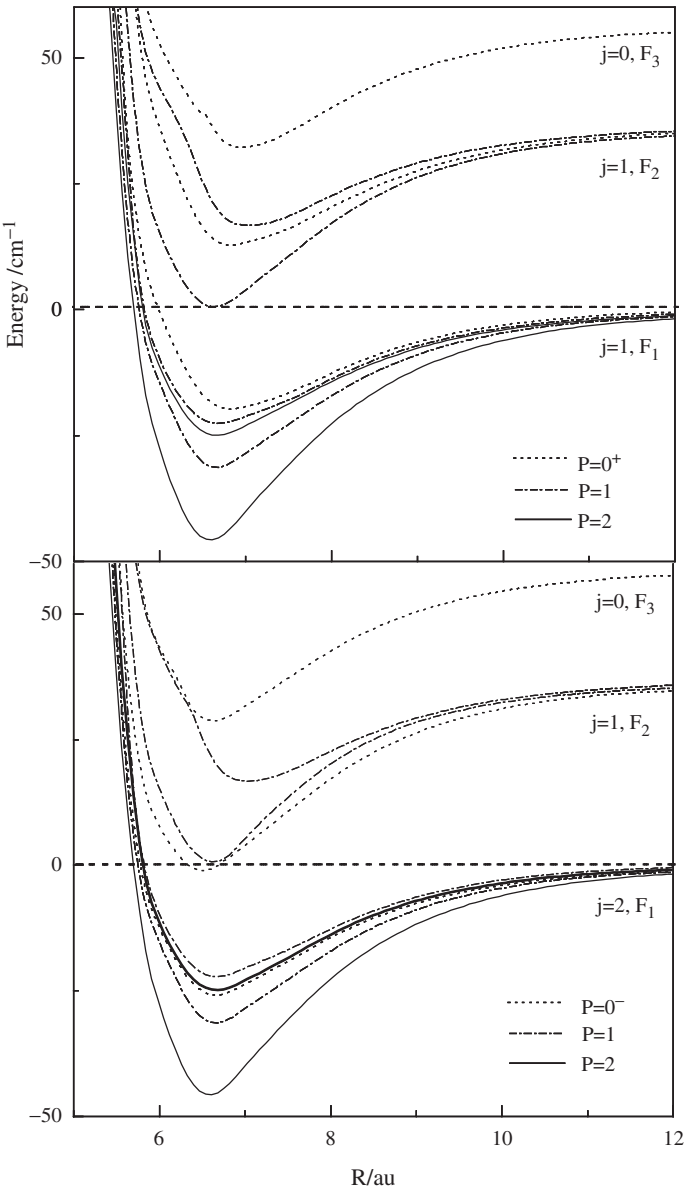

Figure 12. Adiabatic bender potentials for NH(A)–Ne. The upper and lower panels show states of + and − parity, respectively. These curves were calculated for total angular momentum $J=2$. The dissociation asymptotes are labelled by the NH angular momentum (j) and the spin–orbit component.

with the observed line broadening, lies above the NH(A, $j=2$, F_1)+Ne dissociation limit. The calculated binding energy for $P=2_l$, F_1 of $D_0(A)=30.6\,\mathrm{cm}^{-1}$ was below the experimental upper bound, and the rotational constants were in reasonably good agreement with the observed values. The calculations correctly predicted that the $P'=0^-$, F_2 state has the largest rotational constant.

Given that the A and c states of NH arise from a common configuration, it was surprising to find that *ab initio* potentials determined at the same level of theory were not of equivalent quality when evaluated against the experimental data. The theoretical surfaces for the two electronic states are very similar, in keeping with the expectation that they are primarily determined by dispersion and repulsive exchange forces. The experimental data indicate more substantial differences. In future work it will be of interest to see if this behaviour can be reproduced using methods that are more sophisticated in their treatment of the correlation energy.

Recent work on the NH(X)+He interaction potential has been stimulated by the recognition that NH(X) is a promising candidate for studies of ultra-cold molecules. The large rotational constant and magnetic moment of NH(X) are well suited for techniques that entail ^{3}He buffer gas loading followed by evaporative cooling in a magnetic trap [85]. For the radicals to remain in the trap it is essential that the cross-section for Zeeman relaxation induced by collisions with He be extremely small. This cross-section has not been measured, but theoretical calculations [14, 15] indicate that it is a factor of at least 10^4 smaller than the elastic cross-section at temperatures in the range 0.5–1 K. The reliability of this prediction is critically dependent upon the accuracy of the theoretical NH(X)–He potential energy surface. Krems *et al.* [14] and Cybulski *et al.* [15] calculated a two-dimensional potential energy surface for NH(X)+He (RCCSD(T)/*avqz*–BF + CP). The equilibrium parameters of this surface were $\theta_e = 62.3^\circ$, $R_e = 6.33$ au and $D_e = 19.84\,\mathrm{cm}^{-1}$. Bound state calculations showed that only the zero-point level was stable, with a binding energy of $D_0 = 4.4\,\mathrm{cm}^{-1}$. The rotational energies followed the expression $E_{\mathrm{ROT}} = B_0 L(L+1)$ with a rotational constant of $0.321\,\mathrm{cm}^{-1}$. The spin splitting was below $0.01\,\mathrm{cm}^{-1}$ and levels with $L > 3$ were predicted to be unbound. Kerenskaya *et al.* [84] observed the NH–He complex using the A–X transition, hence the NH(A)+He potential energy surfaces were also of interest. Jonas and Staemmler [86] calculated the A state potentials using the correlated electron pair approximation with an augmented, triple zeta quality basis set and CP corrections. Although the focus of this study was on the repulsive regions of the potentials, they noted that there were van der Waals minima for the linear geometries, with a well depth of $D_e = 21\,\mathrm{cm}^{-1}$ for NH–He. Jonas and Staemmler [86] estimated that the D_e value from their calculations would be too small by a factor of 2. Their potentials were used by Neitsch *et al.* [87] to predict inelastic scattering cross-sections for NH(A)+He collisions. Kerenskaya *et al.* [84] used CASPT2/*av6z* calculations to better characterize the attractive regions of the potentials. The resulting surfaces were deeper ($D_e = 40\,\mathrm{cm}^{-1}$) than those of Jonas and Staemmler [86] with a shorter equilibrium bond distance ($R_e = 6.24$ versus 6.6 au). Further details are given in table 4. Despite the fact that $D_e(A)$ was twice the depth of D_e(X), bound state calculations with the new A state potentials yielded a binding energy of $D_0(A) = 3.3\,\mathrm{cm}^{-1}$ that was less than that of the ground state. The steep anisotropy of the potentials in the vicinity of the global minimum was partly responsible for this unusually large zero-point energy. The calculated zero-point rotational constant for the $P = 2_l$ state was $0.303\,\mathrm{cm}^{-1}$. Adiabatic bender curves for NH(A)–He were qualitatively the same as those shown in figure 12 for NH(A)–Ne, with the same energy ordering for the various P states.

Kerenskaya *et al.* [84] obtained NH(X)–He complexes by photolysis of NH_3 in a He free-jet expansion. Source pressures in excess of 25 atm were needed to achieve conditions where viable concentrations of the complex could be generated. The complex was observed in association with the monomer 0–0 and 1–0 transitions. Bands terminating on the $P' = 2_l$ and 1_l states were observed near the monomer $R_{11}(1)$ line. At higher energy a $P' = 0^- - P'' = 0^-$ band was found on the low-frequency side of the monomer $Q_{21}(1)$ line. The lines of this band were broadened by spin–orbit predissociation. The lifetime of the $J = 1$ level for $v = 0$ was approximately 30 ps. Transitions to or from rotational levels with $L > 3$ were not observed. Dissociation limits could not be extracted from the spectra, but the difference between the upper and lower state binding energies of $D_0(A) - D_0(X) = 0.6\,cm^{-1}$ was defined. Taken with the theoretical value for $D_0(X)$ this yields a value of $5.0\,cm^{-1}$ for $D_0(A)$. The discrepancy with the theoretical value can be readily accounted for by small errors in the anisotropy of the A state potentials. A second indication that the anisotropy should be decreased was given by the interval between the $P = 1_l$ and 2_l states. The measured value for this spacing was $1.3\,cm^{-1}$ while the calculations predicted $2.2\,cm^{-1}$. The experimental value for the rotational constant of NH(X)–He was $B_0 = 0.334(2)\,cm^{-1}$. This was larger than the effective rotational constant derived from the theoretical calculations of Cybulski *et al.* [15]. Average bond distances, estimated from the relationship $\langle R^{-2}\rangle^{-1/2} = \sqrt{\hbar^2/2\mu B}$ were 7.71 au (theory) and 7.56 au (exp), which suggests that R_e may be slightly overestimated by the *ab initio* calculations.

Detection of NH(X)–He demonstrated that a bound state of the complex exists and the rotational constant data indicated that the potential energy surface of Cybulski *et al.* [15] is reasonably accurate. However, Cybulski *et al.* [15] have shown that the calculated Zeeman relaxation cross-sections are extremely sensitive to the details of the potential. Further calculations preformed at even higher levels of theory may be needed to confirm convergence of the results for the Zeeman relaxation cross-sections.

4.4. *OH–Rg and SH–Rg complexes*

The OH–Rg complexes are the most extensively studied family of open-shell van der Waals molecules [25, 88]. While the data for SH–Rg complexes are not as complete, they have also been the focus of a good number of studies. A comprehensive review of the spectroscopic and theoretical work for the complexes of OH and SH with Rg = Ne, Ar and Kr has been provided by Carter *et al.* [25]. This covers work published before the year 2000. In the following I will summarize the progress made from 2000 onwards.

The larger part of the experimental data for OH–Rg complexes has been derived from studies of the $A^2\Sigma^+ - X^2\Pi$ transition. As electronic excitation results in a substantial change in the interaction potential, LIF spectra for OH–Rg complexes access a wide range of vibrationally excited levels of the A state. These data have been used to generate empirically refined potential energy surfaces. These exhibit minima for the linear geometries, with the global minimum for OH–Rg. The best available potentials for OH(A)–Ne, Ar, and Kr are still those described by Carter *et al.* [25] (see table 5). Recent progress for the A-state complexes includes theoretical studies of OH(A)–He and OH(A)–Ne, and experimental observations of OH–He.

Table 5. Stationary point data for OH–Rg complexes.

Surface	D_e/cm^{-1}	θ_e	R_e/au	Reference
OH($X^2\Pi$)–He				
$V_{A'}$, *ab initio*	30.02	68.6	5.7	[89]
$V_{A'}$, *ab initio*	27.06	0	6.55	[89]
$V_{A''}$, *ab initio*	27.06	0	6.55	[89]
$V_{A''}$, *ab initio*	21.79	180	6.09	[89]
OH($A^2\Sigma$)–He				
V, *ab initio*	121.9	0	5.28	[89]
V, *ab initio*	51	180	5.13	[89]
OH($X^2\Pi$)–Ne				
$V_{A'}$, *ab initio*	56.65	69.8	5.84	[89]
$V_{A'}$, *ab initio*	53.46	0	6.58	[89]
$V_{A''}$, *ab initio*	53.46	0	6.58	[89]
$V_{A''}$, *ab initio*	44.66	180	6.16	[89]
iv) OH($A^2\Sigma$)–Ne				
V, *ab initio*	229.8	0	5.43	[89]
V, *ab initio*	83.9	180	5.42	[89]
OH($X^2\Pi$)–Ar				
$V_{A'}$, *ab initio*	147.3	0	7.08	[93]
$V_{A''}$, *ab initio*	147.3	0	7.08	[93]
$V_{A''}$, *ab initio*	95.5	180	6.7	[93]
OH($A^2\Sigma$)–Ar				
V, empirical	1096.4	0	5.35	[25]
V, empirical	938.6	180	4.2	[25]
OH($A^2\Sigma$)–Kr				
V, empirical	2418.4	0	5.24	[25]
V, empirical	1900	180	4.16	[25]

Lee *et al.* [89] calculated *ab initio* potential energy surfaces for the A and X states of OH–He and OH–Ne. They used the RCCSD(T) method with *avtz* and *avqz* basis sets. Mid-bond functions were included and the CP correction was applied. Bound state calculations for OH(A)–Ne using the *ab initio* potential gave results that were in reasonable agreement with the experimental data, but the vibrational intervals were systematically underestimated. Better agreement was obtained for the rotational constants. Lee *et al.* [89] found that the prediction of the vibrational energies was optimized when the potential was scaled by a factor of 1.12. The *ab initio* potential for OH(A)–He had the same qualitative form as the potentials for other OH(A)–Rg complexes. The global minimum was located at $D_e = 121.9\,\text{cm}^{-1}$, $R_e = 5.28$ au. Bound state calculations for OH(A)–He yielded a binding energy of $D_0 = 7.12\,\text{cm}^{-1}$ and a rotational constant of $B_0 = 0.3695\,\text{cm}^{-1}$.

Calculations for OH(X)–He predicted that the complex should be bound by $6\,\text{cm}^{-1}$. Han and Heaven [90] recently verified the existence of a stable OH–He complex using the A–X bands. Transitions from the ground state $P = 3/2^+$, $J = 3/2$ level to levels associated with OH(A), $n = 0$, 1 and 2, were observed. The OH–He origin band was red-shifted from the monomer $P_1(3/2)$ parent line by $1.6\,\text{cm}^{-1}$. Unfortunately the rotational structure of this band was obscured by the very intense monomer line.

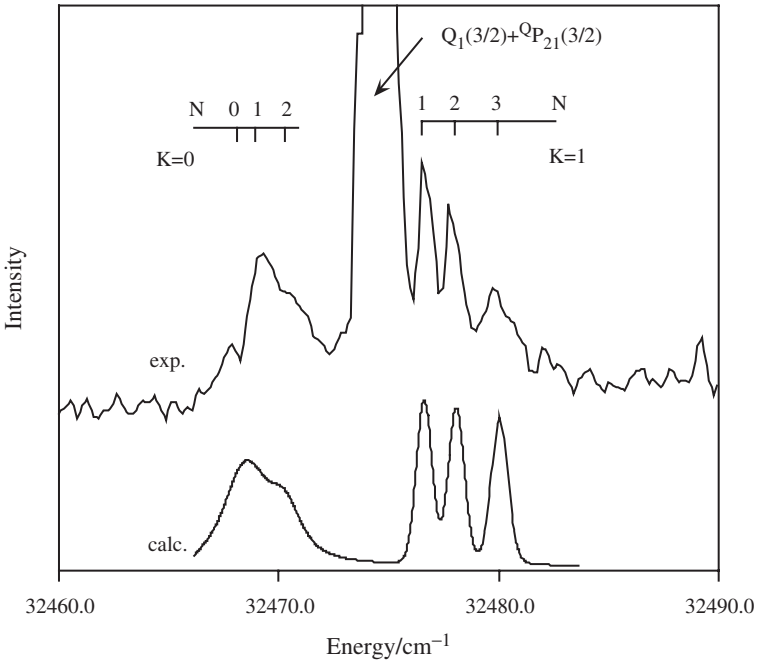

Figure 13. LIF spectrum and scattering resonance simulation for the A–X transition of OH–He. The upper trace shows the spectral features of OH–He associated with the $n=1$ rotational level of OH(A). The intense line in the centre of this spectrum is from the monomer. The lower trace is a simulation of the OH–He spectrum derived from scattering resonance calculations.

The OH–He features associated with the $n=1$ rotational state are shown in figure 13. A similar pattern of complex features, flanking the monomer $R_1(3/2)$ line, was observed for $n=2$. The features associated with $n=1$ and 2 were scattering resonances that were well above the OH(A, $n=0$)+He dissociation asymptote. The *ab initio* potential of Lee *et al.* [89] was used to calculate the resonance energies and widths. Resonances with angular momentum $N=0$, 1, 2, and 3 were predicted for $n=1$. The pattern of energy intervals for these resonances indicated that K was a well-defined quantum number. The $K=0$ resonances had greater widths than those for $K=1$. This was expected as $K=0$ corresponds to rotation of OH in the triatomic plane, where the coupling between the angular and radial motions will be the strongest. The calculated resonances are compared with the experimental spectrum in figure 13. Overall the agreement is good, but the overestimation of the spacing between the $K=0$ and $K=1$ groups suggests that the anisotropy of the potential energy surface should be reduced. Calculated resonances for the $n=2$ group were also in reasonable agreement with the observations. K was not a good quantum number for this group, mostly due to the Coriolis interactions between the zeroth-order $K=0$, 1, and 2 states. The energies of the OH–He transitions, relative to the monomer lines, were consistent with the binding energies calculated by Lee *et al.* [89]. One interesting fact of OH–He is the prediction that electronic excitation increases the D_e from 30 to 122 cm^{-1}, while the D_0 value increases by just 1.1 cm^{-1} (1.6 cm^{-1} observed). This is the consequence of an unusually

large zero-point energy effect in the excited state. Simulation of the spectrum supports this interpretation. A shallower potential surface for OH(A)–He, modified in a way that permits the reduction of D_e while maintaining D_0, would not have sufficient anisotropy at long range to produce the splittings seen in the resonance structures.

In general, the experimental data for the $X^2\Pi$ states of OH–Rg complexes are more limited than those available for the A states. Hence our knowledge of the potential energy surfaces is more heavily dependent on *ab initio* calculations. The most extensive data are for OH(X)–Ne and OH(X)–Ar, where vibrationally excited levels have been characterized using dispersed fluorescence and SEP techniques [34–36]. Additional data for OH(X)–Ar are available from microwave measurements and a high-resolution IR study of bands associated with the OH fundamental [37]. Initially, theoretical calculations for OH(X)–Ne and OH(X)–Ar predicted linear equilibrium geometries for both the A' and A'' surfaces [25, 88]. More recent studies, carried out with higher-level methods and larger basis sets, show that the A' potentials for He and Ne favour bent configurations (see table 5; note that the half-filled $p\pi$ orbital of OH(X) is in the molecular plane for the A' surface and the field orbital is in-plane for A''). Lee *et al.* [89, 91] evaluated the quality of their OH(X)–Ne potentials by calculating vibrational energies, rotational constants and scattering resonances. The results were compared with the experimental data and calculations performed using the potential energy surfaces of Yang *et al.* [54]. The bound state energies and rotational constants were close to the experimental values for both sets of potentials, provided that the Coriolis mixing was taken into account. Although the potentials of Lee *et al.* [89] were quite similar to those of Yang *et al.* [54], the degree of rotor basis state mixing for the potentials was significantly different. Lee *et al.* [89] found that both the Coriolis operator and the difference potential induced considerable mixing of the various zeroth-order P states, while P remained as a good quantum number when the potentials of Yang *et al.* [54] were used. Conflicting predictions for the energy ordering of the $P=3/2^-$ and $1/2^+$ states was one consequence of these differences. Since the $P=3/2^-$ state has not been observed, the true ordering is not yet known. Scattering resonance calculations for OH(X)–Ne yielded similar insights [91]. While the potentials of Yang *et al.* [54] and Lee *et al.* [89] both gave respectable agreement with the measured resonance energies they differed in their predictions for the resonance lifetimes. Due to details of the state mixings, the lifetimes of Lee *et al.* [91] were shorter and showed strong dependencies on the nominal value of P and the parity. Curiously, neither of the model potential sets could reproduce the magnitude of the increase of the resonance lifetimes that accompanied excitation of the van der Waals stretch. From these studies it was evident that the scattering resonances provide a very exacting test of the quality of the potential energy surfaces.

Empirically adjusted potential energy surfaces for OH(X)–Ar were reported in 1993 by Dubernet and Hutson [92]. These surfaces were successful in fitting nearly all of the experimental data available at that time. The one unresolved problem was with the parity splittings for the $P=3/2^+$ and $1/2^+$ states. Dubernet and Hutson [92] found that the ratio of the measured parity splittings could not be obtained with any realistic adjustment of the potentials. This anomaly has since been resolved by Bonn *et al.* [37], who have corrected the experimental value for the $P=1/2^+$ parity splitting constant. In this work, high-resolution IR spectra were recorded for transitions to the $P=3/2^+$

and $1/2^+$ states of OH(X, $v=1$)–Ar. The parity splitting constant for the $P=1/2^+$ state was found to be about three times larger than that derived from the partially resolved SEP spectrum. Bonn *et al.* [37] successfully reinterpreted the SEP data using the revised value for the parity splitting constant. Concurrent with the experimental work, Klos *et al.* [93] calculated new *ab initio* surfaces for OH(X)–Ar using the UMP4 method with an *avtz*–BF basis and CP corrections. The global minimum of the A' surface was found to be linear ($D_e=147.3\,\mathrm{cm}^{-1}$) but this surface also supported a local minimum for a bent geometry ($D_e=135.5\,\mathrm{cm}^{-1}$, $\theta_e=75.1^\circ$) and a saddle point at $\theta=180^\circ$. The A' surface had the usual linear minima, separated by a saddle point near $\theta=105^\circ$ (see table 5). Bound states calculated from these surfaces were in very good agreement with the experimental results, including the $P=1/2^+$ parity splitting. The only notable discrepancy was overestimation of the $P=3/2^+$–$1/2^+$ interval (10.8 versus $9.2\,\mathrm{cm}^{-1}$), indicative of a small error in the anisotropy of the average potential.

Carter *et al.* [25] reviewed the spectroscopic data for SH/D–Ne, Ar, and Kr complexes that had been derived from LIF and dispersed fluorescence studies. Empirical potential energy surfaces were fitted to these data. Guided by the results for OH–Rg complexes, the potentials were constructed with global minima for the linear SH–Rg geometry. During the past few years the characterization of SH–Rg complexes has been advanced by a variety of theoretical calculations, and detailed studies of SH(X)–Rg using microwave techniques. An unexpected general trend was the discovery that the potential energy surfaces for the ground state complexes have linear Rg–SH(X) equilibrium structures. However, the anisotropies of the surfaces are so weak that the vibrationally averaged structures for the zero-point levels favour the SH–Rg geometry.

Ab initio surfaces for the X and A states of He–SH and Ne–SH were calculated by Cybulski *et al.* (RCCSD(T)/*avtz*–BF+CP) [94]. The stationary points for these surfaces are listed in table 6. The A' surfaces exhibited secondary minima for bent configurations and saddle points for linear SH–He/Ne, while the A'' surfaces had two linear minima. The binding energies for SH–He, $D_0(X)=6.2\,\mathrm{cm}^{-1}$, $D_0(A)=6.8\,\mathrm{cm}^{-1}$ were found to be similar to those for OH–He. The SH–He complex has not been observed to date. The potential energy surfaces for SH(X)–Ne were evaluated against the experimental data derived from studies of the A–X transition. Cybulski *et al.* [94] found that their surfaces yielded rotational constants that were in good agreement with the experimental values, and the binding energy of $D_0=31.7\,\mathrm{cm}^{-1}$ was within the experimental error limits. The fit to the bound vibrational energies was respectable, but not quite as good. The dispersed fluorescence data also contained transitions to scattering resonances above the SH(X, $\omega=3/2$, $j=3/2$) + Ne dissociation limit. Lee and McCoy [91] showed that their surfaces could also reproduce the resonance energies. In comparing the properties of SH(X)–Ne with OH(X)–Ne, Lee and McCoy [91] noted that the state mixing induced by the difference potential was less important for SH–Ne. This was a consequence of the larger spin–orbit interaction of SH(X). Suma *et al.* [40] recorded microwave spectra for SH(X)–Ne and used the results to refine the ground state potentials. Their reference potentials were obtained from *ab initio* calculations that were carried out at the same level of theory as the work of Cybulski *et al.* [94]. To fit the microwave data the average potential was adjusted by a slight inward translation and small corrections to the anisotropy that

Table 6. Stationary point data for SH–Rg complexes.

Surface	D_e/cm^{-1}	θ_e	R_e/au	Reference
SH($X^2\Pi$)–He				
$V_{A'}$, *ab initio*	25.97	54.4	6.88	[94]
$V_{A'}$, *ab initio*	25.27	180	6.79	[94]
$V_{A''}$, *ab initio*	25.27	180	6.79	[94]
$V_{A''}$, *ab initio*	21.16	0	7.8	[94]
SH($A^2\Sigma$)–He				
V, *ab initio*	49.3	0	7.09	[94]
V, *ab initio*	69.97	180	5.66	[94]
SH($X^2\Pi$)–Ne				
$V_{A'}$, *ab initio*	57	57.2	6.83	[94]
$V_{A'}$, *ab initio*	54.27	180	6.79	[94]
$V_{A''}$, *ab initio*	54.27	180	6.79	[94]
$V_{A''}$, *ab initio*	45.75	0	7.75	[94]
V_{ave}, modified	53.13	180	6.75	[40]
V_{ave}, modified	48.26	0	7.71	[40]
SH($A^2\Sigma$)–Ne				
V, *ab initio*	103.2	0	7.04	[94]
V, *ab initio*	107.9	180	5.98	[94]
SH($X^2\Pi$)–Ar				
V_{ave}, *ab initio*	121.66	0	8.12	[41]
V_{ave}, *ab initio*	123.67	180	7.26	[41]
V_{ave}, modified	115.81	34.2	7.74	[41]
V_{ave}, modified	121.59	180	7.16	[41]
SH($A^2\Sigma$)–Ar				
V, *ab initio*	742.5	0	6.42	[95]
V, *ab initio*	673.7	180	5.316	[95]
V, empirical	877.2	0	6.46	[25]
SH($X^2\Pi$)–Kr				
V_{ave}, *ab initio*	160.5	41.4	7.89	[40]
V_{ave}, *ab initio*	163.8	180	7.41	[40]
V_{ave}, modified	160.4	46.8	7.76	[25]
V_{ave}, modified	167.5	180	7.37	[25]
SH($A^2\Sigma$)–Kr				
V, empirical	1706.2	0	6.17	[25]

lessened the energy difference between the linear minima. In addition to giving an excellent fit to the microwave data, the adjusted potentials yielded energies for vibrationally excited levels and scattering resonances that were in good agreement with the dispersed fluorescence data. This unusual circumstance, where microwave data for the zero-point level could be used to define the properties of the potentials at locations far from the equilibrium geometry, was a consequence of the large-amplitude motion associated with this level.

Sumiyoshi and Endo [41] carried out a similar study of the microwave spectrum of SH(X)–Ar. Two methods of analysis were employed. First, the microwave transitions were fitted using a traditional effective Hamiltonian. Interesting details of the constants determined by this approach included a negative centrifugal distortion constant and a significantly reduced value for the leading hyperfine coupling constant (as compared

to free SH). The second approach was to fit empirically adjusted potential surfaces to the data. The reference potential for this process was obtained from *ab initio* calculations (RCCSD(T)/*avqz*+CP). The initial form for the average potential had linear minima with well depths of $D_e(0^\circ) = 115\,\mathrm{cm}^{-1}$ and $124\,\mathrm{cm}^{-1}$ (180°). The fitted potential was less deep by $2\,\mathrm{cm}^{-1}$ for $\theta = 180^\circ$, but the critical adjustment was reduction of the well depth and anisotropy of the potential near $\theta = 0^\circ$ ($D_e(0^\circ) = 108\,\mathrm{cm}^{-1}$). These changes were needed to reproduce the negative centrifugal distortion constant. The leading term of the difference potential was reduced by 15%. The fitted potentials reproduced the hyperfine splittings of the spectrum using the unmodified hyperfine constants for free SH. Hence it was shown that the smaller constant obtained from the fit to the effective Hamiltonian was influenced by vibrational averaging, rather than a tangible perturbation of the SH electronic structure.

Ab initio calculations for SH(*A*)–Ar were reported recently by Hirst *et al.* [95] (RCCSD(T)/*av5z*+CP). Details of this surface are given in table 6. The rotational constants and binding energy ($D_0 = 446.7\,\mathrm{cm}^{-1}$) were in agreement with the experimental data, while the vibrational intervals were underestimated by about 5%. All of the observed levels of SH(*A*)–Ar have been assigned to states that are localized in the $\theta = 0^\circ$ well, and this was confirmed by Hirst *et al.* [95]. However, they also found that several bound states were supported by the $\theta = 180^\circ$ well. They discussed the possibility that electronic predissociation of the latter may have precluded the observation of these states in previous experiments, where the detection of long-lived fluorescence was used to discriminate against the monomer spectrum.

The microwave spectrum of SH(*X*)–Kr was recorded by Suma *et al.* [40]. The data were analysed by direct fitting of the potential energy surfaces. Potentials obtained from CCSD(T)/*avqz*+BF+CP calculations were used for the initial estimate. The average potential for SH–Kr was a little different from those for –Ne and –Ar in that the secondary minimum corresponded to a bent configuration with θ near 50°. The well depths for the linear minima were $D_e(0^\circ) = 156\,\mathrm{cm}^{-1}$ and $D_e(180^\circ) = 164\,\mathrm{cm}^{-1}$ (calculated). Differences between the average *ab initio* surface and the fitted potential were most noticeable near the linear minima. The well depth at 0° was decreased by $3\,\mathrm{cm}^{-1}$ while that at 180° was increased by $3\,\mathrm{cm}^{-1}$. The leading term of the difference potential was decreased by 5% and the surfaces translated inwards by 0.04 au. Vibrationally excited levels of SH(*X*)–Kr have not yet been observed, and Suma *et al.* [40] did not report predictions for these levels based on their adjusted potentials.

5. Complexes of HX radicals with multiple Rg atoms

Open-shell molecules interacting with small clusters of rare gas atoms provide useful model systems for studies of the solvation of radicals, the energy level structures associated with solvated radicals, and the relative importance of many-body effects in determining the potential energy surfaces for clusters with multiple interacting partners. The experimental data for Rg_n–HX clusters are rather sparse at present. The frequencies for *A*–*X* vibronic bands of the OH/D–Ne_n complexes with $n = 2 - 4$ were reported by Lin *et al.* [96]. Miller and co-workers [97] recorded rotationally resolved electronic spectra for OH/D–Ne_2, but the analysis of these data has not been completed.

Large CH–Ar_n clusters ($n \approx 50$) have been observed in association with the A–X transition [98]. Despite the lack of data, there have been a number of interesting theoretical studies of Rg_n–HX complexes. This work has been stimulated by the availability of good-quality potential energy surfaces for the binary complexes, and it parallels the extensive studies of closed-shell Rg_n–HX complexes that have been carried out in recent years [16–21].

A model for the interaction of a molecule in a $^2\Pi$ state interacting with multiple rare gas atoms has been developed by Xu *et al.* [22, 99, 100] They represent the components of the potential energy surfaces that arise from the Rg–HX interactions in terms of the matrix

$$V_{RgHX} = \begin{pmatrix} V_I & V_{II} \\ V_{II}^* & V_i \end{pmatrix} \tag{7}$$

where

$$V_I = \langle \pm\lambda | V | \pm\lambda \rangle = \sum_{k=1}^{n} V_{\text{ave}}(R_k, \theta_k) \tag{8}$$

$$V_{II} = \langle \pm\lambda | V | \mp\lambda \rangle = \sum_{k=1}^{n} V_{\text{diff}}(R_k, \theta_k) \exp(-2\lambda i \phi_k) \tag{9}$$

and R_k, θ_k and ϕ_k are the polar coordinates for the k-th atom. To obtain the complete potentials the pairwise interactions between the Rg atoms and the spin–orbit interaction energies are added to the diagonal elements of equation (7), and the resulting matrix is diagonalized. Xu *et al.* [100] first applied this model to CH(X)–Ar_n complexes with $n = 2$–15. Simulated annealing and Newton–Raphson minimization techniques were used to locate minimum energy structures. The structure for the CH–Ar_2 complex was found to be dramatically different from the structures of closed-shell Ar_2–HX clusters or the open-shell Ar_2–NO($^2\Pi$) complex. In the latter the Ar atoms form a dimer that interacts with HX or NO. However, CH(X)–Ar_2 has a planar equilibrium structure with the Ar atoms on either side of the C atom. This configuration loses the stabilization energy from the Ar–Ar interaction, but this is more than offset by the energy gained by allowing both Ar atoms to approach along the axis of the empty $p\pi$ orbital, thereby accessing the deepest minimum of the Ar–CH potential energy surface. This stable CH–Ar_2 unit has a strong influence on the structures of the complexes with $n = 3$ and 5–11. While the analogous closed-shell complexes had the form of HX interacting with a Rg_n cluster, the interaction with CH distorted the Rg_n cluster to incorporate the stable CH–Ar_2 structure (the energy advantage of making a tetrahedral Ar_4 cluster wins out for $n = 4$). For $n = 12$–15 the minimum energy structures preserved the CH–Ar_2 motif, but this unit was found at the surface of the cluster as this minimizes the disruption of the remaining Ar–Ar interactions. This study clearly demonstrated that the factors influencing the solvation of an

open-shell molecule can be qualitatively different from those that govern closed-shell systems. The insights gained from the calculations of Xu *et al.* [100] also shed light on the opposing spectral shifts observed for CH–Ar_n clusters and matrix isolated CH. As described in the section on binary clusters, the electronic origin band for the *A–X* transition of CH–Ar is blue-shifted relative to that of the monomer. Burroughs *et al.* [98] found that the cluster spectrum remained blue-shifted as the cluster size was increased (the largest clusters examined were estimated to contain about 50 Ar atoms). However, the *A–X* transition of CH isolated in a solid Ar matrix was red-shifted relative to free CH by $31\,cm^{-1}$. The *B–X* transition also shows a blue-shift for CH–Ar and a red-shift in an Ar matrix [98]. In part, these opposing trends can be understood in terms of the stabilization of the ground state. By placing the CH on the outer surface, the CH–Ar_n clusters can adopt structures that maximize the attractive interaction with the empty $p\pi$ orbital, and minimize repulsive interactions with the half-filled orbital. In the matrix, CH is embedded in the rare gas solid and the lattice opposes the symmetry-breaking optimization of the solvent cage. This will destabilize CH(*X*) in the matrix, thereby contributing to the observed red-shift.

OH($X^2\Pi$)–Ar_n clusters with $n = 2$–15 were examined by Xu *et al.* [99]. Their study offers an interesting contrast to the work on CH–Ar_n as the equilibrium structure for the binary complex is linear, and the magnitude of the spin–orbit coupling constant for OH is larger than that for CH ($-139\,cm^{-1}$ versus $28\,cm^{-1}$). The OH(*X*)–Ar_n cluster geometries were found to be similar to those of Ar_n–HCl. For $n < 10$ they corresponded to symmetric Ar_{n+1} clusters, with one of the Ar's replaced by OH. For example, the lowest energy form of OH–Ar_4 could be derived from the trigonal bipyramid form of Ar_5 by substituting OH for one of the equatorial Ar's (C_{2v} symmetry). The next lowest energy structure was obtained by substituting for one of the axial Ar atoms (C_{3v} symmetry). High-symmetry structures were predicted, indicating that the moderately large spin–orbit interaction of OH had suppressed the expected Jahn–Teller distortion. An abrupt change in the structure occurred for $n = 10$, where the OH was located inside an incomplete icosahedral cage. The addition of further Ar atoms completed the cage and began the formation of a second solvation sphere. In contrast to the behaviour of CH in Ar, OH could be incorporated within a symmetric cage due to the smaller difference potential and stronger spin–orbit coupling.

Having located the minimum energy structures for OH(*X*)–Ar_n, Xu *et al.* [22] went on to examine the quantized vibrational states of the clusters with $n = 4$–12 using large-scale variational calculations. To reduce the problem to manageable dimensions, the Ar cage was frozen. The OH centre of mass and polar angles were treated as free variables (five-dimensional motion on two potential energy surfaces). The evolution of the OH bending and translation energy levels was followed as a function of cluster size. As expected, the smaller clusters exhibited splittings of the various *P* states that were qualitatively similar to the pattern for OH(*X*)–Ar. The vibrational frequencies for the translational modes increased with the cluster size. The incorporation of OH inside the cluster at $n = 10$ had a dramatic effect on the energy levels of the bending mode. Demonstrating a beautiful complementarity, the bending levels for the $n = 10$ and 11 clusters were inverted forms of the patterns for OH–Ar_2 and OH–Ar. Here the atoms missing from the icosahedral cage acted as holes in an otherwise symmetric environment. Symmetry dictates that the spatial degeneracy of the OH *j*-levels should

not be broken is an icosahedral cage. The calculations were essentially in agreement with this expectation, but small splittings were predicted as the rigid cage from the cluster optimization was slightly distorted. The frequency in the translation mode was about 60 cm^{-1} for the closed cage. Xu *et al.* [22] noted that the rigid cage model would not be successful for CH(X)–Ar_n as the distortion of the cage caused by the empty $p\pi$ orbital would need to be able to follow the CH for motions involving internal rotation.

Theoretical studies of SH(A)–Ne_n and OH(A)–Ne_n have been carried out by Lee *et al.* [101–103]. As the radicals are in the orbitally non-degenerate $^2\Sigma^+$ state, these clusters can be treated as closed-shell systems to a good approximation. In their first papers on this problem, Lee *et al.* [102, 103] examined SH(A)–Ne_n and OH(A)–Ne_n clusters with $n = 1$–4 to evaluate the suitability of adiabatic diffusion Monte Carlo (ADMC) methods for calculations of the bound state properties. The advantage of this method is that it has favourable computational scaling for the treatment of moderately large systems. The disadvantage is that it is difficult to treat vibrationally excited levels using ADMC as prior knowledge of the nodal surfaces of the wavefunctions is required.

The equilibrium structures of SH(A)–Ne_n and OH(A)–Ne_n clusters were determined for additive pair-potential models that used empirical potential energy surfaces for the SH(A)–Ne and OH(A)–Ne interactions. The minimum-energy structures were consistent with the HX moiety interacting with a symmetric Ne_n cluster. For $n = 2$ the T-shaped Ne_2–HX complexes with the H atom pointing towards the mid-point of the Ne–Ne bond (C_{2v} symmetry) were lowest in energy. The next two isomers were linear Ne–HX–Ne and NeNe–HX. The global minimum for Ne_3–HX was the tetrahedral-like structure (C_{3v} symmetry) with T-shaped Ne_2–HS–Ne (C_{2v}) as the next most stable structure. The complexes for $n = 4$ yielded different equilibrium structures for SH and OH. Both were based on a Ne_5 trigonal bipyramid with one of the equatorial Ne's replaced by the HX group. However, for SH–Ne_4 the H atom points towards the mid-point of the remaining equatorial Ne's (C_{2v}) while for OH the H atom points towards one of the facets of the trigonal bipyramid (C_s symmetry). The next lowest energy isomer for both SH and OH was the bipyramid with substitution of one of the axial Ne's (C_{3v}).

ADMC calculations for the vibrational ground states of the clusters showed that the zero-point energies were always a substantial fraction of the classical dissociation energy for HX–$Ne_n \rightarrow$ HX+nNe. The factor $(D_e - D_0)/D_e$ was greater than 0.4 for all of the clusters examined. From analyses of the wavefunctions and rotational constants, Lee *et al.* [101, 103] were able to show that the average structures for the zero-point levels were close to those of the global minimum energy structures, despite the fact that the barriers between low-lying minima were below the zero-point energies. Calculations for vibrationally excited levels of Ne_2–HX were reported. For the Ne_2–SH complex the five vibrational modes of the T-shaped isomer were characterized. Similar results were obtained for Ne_2–OH, with one interesting difference. Calculations for the OH in-plane bending fundamental exhibited convergence problems that were traced to the existence of a nearby state belonging to an excited bending level of the linear Ne–HO–Ne isomer. Variational calculations for SH–Ne_2 and OH–Ne_2 were used to evaluate the validity of the ADMC results. Lee *et al.* [102] determined the energies of the first 25 vibrational levels of both complexes. Good agreement between the

variational energies and those from ADMC was obtained for the zero-point energies and the fundamentals for the T-shaped isomers. Vibrational progressions belonging to other distinguishable isomers were also predicted by the variational calculations. These included the levels of the two linear isomers (Ne–HX–Ne and NeNe–HX) and an unusual combination state with an average structure that was L-shaped. The density of states for the Ne_2–HX complexes was found to be of the order of one vibrational state per waveneumber. Fortunately, the spectroscopic data indicate that very few of these modes are active in the *A–X* spectra, so it has been possible to obtain well-resolved data. The rich dynamical behaviour expected of the Ne_2–HX complexes is sufficiently intriguing to justify the additional efforts that will be needed to assign the existing data and extend the spectroscopic characterization of these complexes.

6. Conclusions and future directions

Extensive experimental and theoretical studies of the Rg–HX complexes have provided a clear picture of the factors that govern the interaction potential energy surfaces and the ro-vibronic energy level patterns that develop from the coupling of the electronic and nuclear degrees of freedom. It is apparent that the interaction forces are predominantly physical in nature, even when the radical is in an electronically excited valence state. Consequently, the general characteristics of the potential energy surfaces are determined by the physical properties of the radical. The electronic configuration of the radical is a particularly important factor, to the extent that the topologies of the potential energy surfaces, and the relative magnitude of the difference potential for orbitally degenerate states, can be anticipated from knowledge of the orbital occupation. One example of this trend is the observation that the electronic states of an Rg–HX complex that are derived from a common electronic configuration have very similar potential energy surfaces.

Current *ab initio* electronic structure methods are capable of predicting good-quality potential energy surfaces for the ground and electronically excited states of Rg–HX complexes. However, it is essential that the calculations be carried out using a sophisticated treatment of the correlation energy, a large basis set, and corrections for the basis set superposition errors. RCCSD(T) calculations with basis sets that include mid-bond functions have been very successful. Bound state calculations using these surfaces yield predictions that are close enough to the observed spectral patterns that they can be used to establish reliable assignments. Small adjustments of the potentials typically yield energy level spacings and rotational constants that reproduce the experimental results. For some of the Rg–HX complexes reported here the analyses of the spectra are incomplete because the correlations between the theoretically predicted energy levels and the observed transitions were ambiguous. It is probable that most of these problems could be traced to the use of electronic structure calculations that were not of sufficient accuracy, and that further progress could be made by recomputing the potentials using higher-level methods with larger basis sets. Ground state potential energy surfaces derived by fitting to microwave data appear to be accurate, but there are few examples where the ability of these surfaces to predict vibrationally excited levels can be tested against experimental data.

Further measurements using SEP and high-resolution IR techniques are needed to develop and validate the ground state potentials. Note that the conclusion that Rg–HX radical complexes are physically bound is based on data for the complexes where Rg = He through Kr. There is evidence from matrix isolation [104] and gas phase emission spectroscopy [105] that indicates chemical bonding for OH–Xe (similar matrix evidence exists for chemically bound Xe–CN [106] and Xe–C_2 [107]). It is possible that several of the Xe–HX complexes will exhibit incipient chemical bonds.

Now that accurate potential energy surfaces are becoming available for many Rg–HX pairs, the foundation has been laid for studies of clusters that contain multiple rare gas atoms. Although this topic has not received much attention from the experimentalists, it is evident that spectroscopic studies of larger clusters are feasible using established techniques. The fact that hydride radicals still emit fluorescence when trapped in rare gas solids shows that non-radiative relaxation processes will not preclude the application of techniques that rely on LIF detection. Hence the clusters can be characterized using electronic spectroscopy and UV–IR double resonance. Theoretical methods for treatment of the dynamics of Rg_n–HX clusters are being developed and the results of calculations for CH–Ar_n and OH–Rg_n complexes show that the properties of open-shell clusters are qualitatively different from those of their closed-shell counterparts. Future studies of the Rg_n–HX clusters should provide detailed insights concerning the way in which an inert solvent cage influences the properties of a reactive molecular fragment. Eventually it is hoped that the results from such studies will facilitate the transfer of our extensive knowledge of gas-phase reaction dynamics to the problems of reactions occurring in solution.

Acknowledgements

Thanks go to Drs Galina Kerenskaya, Anatoly Komissarov, Alexey Kaledin, Jiande Han and Udo Schnupf for their contributions to the Rg–HX studies carried out at Emory University. Support from the National Science Foundation (grant CHE-0213313) for the Emory component of the research described here is gratefully acknowledged.

References

[1] D. Skouteris, D. E. Manolopoulos, W. Bian, H.-J. Werner, L.-H. Lai, and K. Liu, Science **286,** 1713 (1999).
[2] P. J. Dagdigian, Advanced Series phys. Chem. **6,** 315 (1995).
[3] P. J. Dagdigian, Ann. Rev. phys. Chem. **48,** 95 (1997).
[4] M. H. Alexander, Chem. Phys. **92,** 337 (1985).
[5] M. H. Alexander and G. C. Corey, J. chem. Phys. **84,** 100 (1986).
[6] P. J. Dagdigian, M. H. Alexander, and K. Liu, J. chem. Phys. **91,** 839 (1989).
[7] K. Liu, R. G. Macdonald, and A. F. Wagner, Int. Rev. phys. Chem. **9,** 187 (1990).
[8] G. Chalasinski and M. M. Szczesniak, Chem. Rev. **100,** 4227 (2000).
[9] J. M. Merrit, J. Kupper, and R. E. Miller, Phys. Chem. chem. Phys. **7,** 67 (2005).
[10] J. Kupper, J. M. Merritt, and R. E. Miller, J. chem. Phys. **117,** 647 (2002).
[11] J. P. Toennies and A. F. Vilesov, Angewandte Chemie, International Edition **43,** 2622 (2004).
[12] S. Y. T. van de Meerakker, P. H. M. Smeets, N. Vanhaecke, R. T. Jongma, and G. Meijer, Phys. Rev. Lett. **94,** 023004 (2005).

[13] D. Egorov, W. C. Campbell, B. Friedrich, S. E. Maxwell, E. Tsikata, L. D. van Buuren, and J. M. Doyle, Eur. Phys. J. D **31,** 307 (2004).
[14] R. V. Krems, H. R. Sadeghpour, A. Dalgarno, D. Zgid, J. Klos, and G. Chalasinski, Phys. Rev. A: Atomic, Molecular, and Optical Physics **68,** 051401/1 (2003).
[15] H. Cybulski, R. V. Krems, H. R. Sadeghpour, A. Dalgarno, J. Klos, G. C. Groenenboom, A. van der Avoird, D. Zgid, and G. Chalasinski, J. chem. Phys. **122,** 094307 (2005).
[16] A. Ernesti and J. M. Hutson, Phys. Rev. A: Atomic, Molecular, and Optical Physics **51,** 239 (1995).
[17] Z. Bacic, J. Chem. Soc. **93,** 1459 (1997).
[18] J. M. Hutson, S. Liu, J. W. Moskowitz, and Z. Bacic, J. chem. Phys. **111,** 8378 (1999).
[19] M. Xu, H. Jiang, and Z. Bacic, J. chem. Phys. **121,** 11045 (2004).
[20] A. McIlroy, R. Lascola, C. M. Lovejoy, and D. J. Nesbitt, J. phys. Chem. **95,** 2636 (1991).
[21] K. Nauta and R. E. Miller, J. chem. Phys. **115,** 10138 (2001).
[22] M. Xu, Z. Bacic, and J. M. Hutson, J. chem. Phys. **117,** 4787 (2002).
[23] Y. Kim and H. Meyer, Int. Rev. phys. Chem. **20,** 219 (2001).
[24] M. D. Wheeler, D. T. Anderson, and M. I. Lester, Int. Rev. phys. Chem. **19,** 501 (2000).
[25] C. C. Carter, H. S. Lee, A. B. McCoy, and T. A. Miller, J. mol. Struct. **525,** 1 (2000).
[26] J. Klos, M. M. Szczesniak, and G. Chalasinski, Int. Rev. phys. Chem. **23,** 541 (2004).
[27] M. C. Heaven, Ann. Rev. phys. Chem. **43,** 283 (1992).
[28] Y. Endo, H. Kohguchi, and Y. Ohshima, Faraday Discuss. **97,** 341 (1994).
[29] Y. Ohshima, M. Lida, and Y. Endo, J. chem. Phys. **95,** 7001 (1991).
[30] S. R. Mackenzie, O. Votava, J. R. Fair, and D. J. Nesbitt, J. chem. Phys. **105,** 11360 (1996).
[31] S. R. Mackenzie, O. Votava, J. R. Fair, and D. J. Nesbitt, J. chem. Phys. **110,** 5149 (1999).
[32] B. C. Chang, L. Yu, D. Cullin, B. Rehfuss, J. Williamson, T. A. Miller, W. M. Fawzy, X. Zheng, S. Fei, and M. C. Heaven, J. chem. Phys. **95,** 7086 (1991).
[33] J. Schleipen, L. Nemes, and J. J. ter Meulen, Chem. Phys. Lett. **175,** 56 (1990).
[34] M. I. Lester, W. H. Green, Jr., C. Chakravarty, and D. C. Clary, Advanced Series phys. Chem. **4,** 659 (1995).
[35] C.-C. Chuang, P. M. Andrews, and M. I. Lester, J. chem. Phys. **103,** 3418 (1995).
[36] M. T. Berry, R. A. Loomis, L. C. Giancarlo, and M. I. Lester, J. chem. Phys. **96,** 7890 (1992).
[37] R. T. Bonn, M. D. Wheeler, and M. I. Lester, J. chem. Phys. **112,** 4942 (2000).
[38] D. T. Anderson, R. L. Schwartz, M. W. Todd, and M. I. Lester, J. chem. Phys. **109,** 3461 (1998).
[39] Y. Ohshima, K. Sato, Y. Sumiyoshi, and Y. Endo, J. Am. Chem. Soc. **127,** 1108 (2005).
[40] K. Suma, Y. Sumiyoshi, and Y. Endo, J. chem. Phys. **120,** 6935 (2004).
[41] Y. Sumiyoshi, Y. Endo, and Y. Ohshima, J. chem. Phys. **113,** 10121 (2000).
[42] Y. Sumiyoshi, Y. Endo, and Y. Ohshima, J. mol. Spectrosc. **222,** 22 (2003).
[43] A. F. Wagner, T. H. Dunning, and R. A. Kok, J. chem. Phys. **100,** 1326 (1994).
[44] M. H. Alexander, S. Gregurick, P. J. Dagdigian, G. W. Lemire, M. J. McQuaid, and R. C. Sausa, J. chem. Phys. **101,** 4547 (1994).
[45] S. Cybulski, G. Chalasinski, and M. M. Szczesniak, J. chem. Phys. **105,** 9525 (1996).
[46] M. L. Dubernet, D. Flower, and J. M. Hutson, J. chem. Phys. **94,** 7602 (1991).
[47] M. H. Alexander, S. Gregurick, and P. J. Dagdigian, J. chem. Phys. **101,** 2887 (1994).
[48] C. Chakravarty and D. C. Clary, J. chem. Phys. **94,** 4149 (1990).
[49] W. H. Green, Jr., and M. I. Lester, J. chem. Phys. **96,** 2573 (1992).
[50] M. L. Dubernet, P. A. Tuckey, and J. M. Hutson, Chem. phys. Lett. **193,** 355 (1992).
[51] U. Schnupf, J. M. Bowman, and M. C. Heaven, Chem. phys. Lett. **189,** 487 (1992).
[52] J. M. Bowman, B. Gazdy, P. Schafer, and M. C. Heaven, J. phys. Chem. **94,** 2226 (1990).
[53] M. Yang, M. H. Alexander, C.-C. Chuang, R. W. Randall, and M. I. Lester, J. chem. Phys. **103,** 905 (1995).
[54] M. Yang and M. H. Alexander, J. chem. Phys. **103,** 3400 (1995).
[55] M. Yang, M. H. Alexander, S. Gregurick, and P. J. Dagdigian, J. chem. Phys. **102,** 2413 (1995).
[56] J. M. Hutson, J. chem. Phys. **91,** 4448 (1989).
[57] G. Kerenskaya, A. L. Kaledin, and M. C. Heaven, J. chem. Phys. **115,** 2123 (2001).
[58] G. Kerenskaya, U. Schnupf, W. H. Basinger, and M. C. Heaven, J. chem. Phys. **123,** 054304 (2005).
[59] M. Meuwly and J. M. Hutson, J. chem. Phys. **110,** 8338 (1999).
[60] M. M. Law and J. M. Hutson, Comp. Phys. Comm. **102,** 252 (1997).
[61] E. Hwang and P. J. Dagdigian, J. chem. Phys. **101,** 2903 (1994).
[62] E. Hwang and P. J. Dagdigian, J. chem. Phys. **102,** 2426 (1995).
[63] M. Kind, F. Stuhl, Y.-R. Tzeng, M. H. Alexander, and P. J. Dagdigian, J. chem. Phys. **114,** 4479 (2001).
[64] B. Nizamov and P. J. Dagdigian, J. phys. Chem. A **107,** 2256 (2003).
[65] M. H. Alexander, W. R. Kearney, and A. F. Wagner, J. chem. Phys. **100,** 1338 (1994).
[66] M. H. Alexander and P. J. Dagdigian, J. chem. Phys. **101,** 7468 (1994).
[67] S. M. Ball, G. Hancock, and M. R. Heal, J. Chem. Soc. Faraday Trans. **90,** 1467 (1994).

[68] S. M. Ball, G. Hancock, and M. R. Heal, J. Chem. Soc. Faraday Trans. **90,** 523 (1994).
[69] G. Richmond, M. L. Costen, and K. G. McKendrick, J. phys. Chem. A **109,** 542 (2005).
[70] C.-C. Wang, Y.-P. Chen, T.-L. Chin, H.-Y. Huang, and K.-C. Lin, J. chem. Phys. **112,** 10204 (2000).
[71] J. L. Cooper and J. C. Whitehead, J. Chem. Soc., Faraday Trans. **89,** 1287 (1993).
[72] H. J. Crichton, C. Murray, and K. G. McKendrick, Phys. Chem. chem. Phys. **4,** 5768 (2002).
[73] J. L. Cooper and J. C. Whitehead, J. phys. Chem. **98,** 8274 (1994).
[74] G. W. Lemire, M. J. McQuaid, A. J. Kotlar, and R. C. Sausa, J. chem. Phys. **99,** 91 (1993).
[75] M. J. McQuaid, G. W. Lemire, and R. C. Sausa, Chem. phys. Lett. **210,** 350 (1993).
[76] A. V. Komissarov and M. C. Heaven, J. chem. Phys. **113,** 1775 (2000).
[77] W. H. Basinger, W. G. Lawrence, and M. C. Heaven, J. chem. Phys. **103,** 7218 (1995).
[78] Schnupf, U. 1995. *Ab initio study of triatomic open shell van der Waals complexes*. PhD Thesis, Emory University, Atlanta.
[79] G. Jansen and B. A. Hess, Chem. phys. Lett. **192,** 21 (1992).
[80] R. A. Kendall, G. Chalasinski, J. Klos, R. Bukowski, M. W. Severson, M. M. Szczesniak, and S. M. Cybulski, J. chem. Phys. **108,** 3235 (1998).
[81] R. W. Randall, C.-C. Chuang, and M. I. Lester, Chem. phys. Lett. **200,** 113 (1992).
[82] G. Kerenskaya, U. Schnupf, and M. C. Heaven, J. chem. Phys. **119,** 8424 (2003).
[83] G. Kerenskaya, U. Schnupf, M. C. Heaven, A. van der Avoird, and G. C. Groenenboom, Phys. Chem. chem. Phys. **7,** 846 (2005).
[84] G. Kerenskaya, U. Schnupf, M. C. Heaven, and A. van der Avoird, J. chem. Phys. **121,** 7549 (2004).
[85] S. Y. T. van de Meerakker, R. T. Jongma, H. L. Bethlem, and G. Meijer, Phys. Rev. A **64,** 041401/1 (2001).
[86] R. Jonas and V. Staemmler, Z. Phys. D. Atoms, Molecules and Clusters **14,** 143 (1989).
[87] L. Neitsch, F. Stuhl, P. J. Dagdigian, and M. H. Alexander, J. chem. Phys. **104,** 1325 (1996).
[88] M. C. Heaven, J. phys. Chem. **97,** 8567 (1993).
[89] H.-S. Lee, A. B. McCoy, R. R. Toczylowski, and S. M. Cybulski, J. chem. Phys. **113,** 5736 (2000).
[90] J. Han and M. C. Heaven, J. chem. Phys. **123,** 064307 (2005).
[91] H.-S. Lee and A. B. McCoy, Phys. Chem. chem. Phys. **4,** 1564 (2002).
[92] M. L. Dubernet and J. M. Hutson, J. chem. Phys. **99,** 7477 (1993).
[93] J. Klos, G. Chalasinski, M. T. Berry, R. A. Kendall, R. Burcl, M. M. Szczesniak, and S. M. Cybulski, J. chem. Phys. **112,** 4952 (2000).
[94] S. M. Cybulski, R. R. Toczylowski, H.-S. Lee, and A. B. McCoy, J. chem. Phys. **113,** 9549 (2000).
[95] D. M. Hurst, R. J. Doyle, and S. R. Mckenzie, Phys. Chem. chem. Phys. **6,** 5463 (2004).
[96] Y. Lin, S. Fei, X. Zheng, and M. C. Heaven, J. chem. Phys. **96,** 5020 (1992).
[97] Miller, T. A. private communication.
[98] A. Burroughs and M. C. Heaven, J. phys. Chem. A **104,** 3842 (2000).
[99] M. Xu, Z. Bacic, and J. M. Hutson, J. chem. Phys. **117,** 4777 (2002).
[100] M. Xu, Z. Bacic, and J. M. Hutson, Faraday Discuss **118,** 405 (2001).
[101] H.-S. Lee, J. M. Herbert, and A. B. McCoy, J. chem. Phys. **111,** 9203 (1999).
[102] H.-S. Lee and A. B. McCoy, J. chem. Phys. **116,** 9677 (2002).
[103] H.-S. Lee and A. B. McCoy, J. chem. Phys. **114,** 10278 (2001).
[104] J. Goodman and L. E. Brus, J. chem. Phys. **67,** 4858 (1977).
[105] H. M. R. Hutchinson, Chem. phys. Lett. **54,** 359 (1978).
[106] A. Thoma, G. Schallmoser, A. M. Smith, B. E. Wurfel, and V. E. Bondybey, J. chem. Phys. **100,** 5387 (1994).
[107] M. Frankowski, A. M. Smith-Gicklhorn, and V. E. Bondybey, Can. J. Chem. **82,** 837 (2004).